공학박사학위논문

Dynamics of temperature sensitive wax dispersion in micro/macroscale over a wide range of volume fraction

광범위한 체적 분율의 왁스 분산계에 대한 미시적/거시적 동역학 연구

2019년 2월

서울대학교 대학원
화학생물공학부
윤 지 원

Abstract

Dynamics of temperature sensitive wax dispersion in micro/macroscale over a wide range of volume fraction

Yoon, Jiwon

School of Chemical and Biological Engineering

Seoul National University

We study the Brownian thermal motion of a colloidal model system made by emulsifying hot liquid α-eicosene wax into an aqueous surfactant solution of sodium dodecyl sulfate (SDS). When this waxy oil-in-water emulsion is cooled below melting point of α-eicosene, T_c ~ 24.6 ℃, the microscale emulsion droplets solidify, effectively yielding a dispersed particulate system. Meanwhile, above T_c, the system works as a good model emulsion. So, the wax droplets can be tuned from a viscous liquid to an elastic solid through very modest changes in absolute temperature.

In the study, we analyze the dynamic and optical properties of dense α-eicosene suspensions at two selected temperatures, T = 10/15 ℃ and T = 30 ℃. These temperatures are chosen far away from T_c. We discuss the effect of changes in the particle deformability, from soft to hard, on the properties of

these emulsions using two different apparatus.

Using the multiple light scattering technique of diffusing wave spectroscopy (DWS), which is very sensitive to small-scale motion and shape fluctuations of dispersed colloidal objects, we show that the thermal fluctuations of the interfaces of these liquid droplets at higher temperature, seen in the DWS intensity–intensity correlation function at early times, effectively disappear when these droplets solidify at lower temperature and the thermal motion can be attributed to the center of mass displacement alone. This transition is fully reversible and therefore particle softness that manifests itself via shape fluctuations of the droplets can be dialed in and out at will. Thus, this system could potentially provide an interesting playground for the concepts of the glass and the jamming transition in even denser suspensions that critically rely on the softness of constituent particles. Here, we show that the early-time behavior of this DWS correlation function can be used to probe mechanical properties of viscoelastic soft materials dispersed as droplets.

The volume fraction regime is categorized into 3 parts in the discussion part. First is under 35 vol%, which is defined as the low volume fraction regime and microstructural changes is observed by diffusion coefficient, and the macroscopic properties are observed by viscosity. Second, the intermediate volume fraction regime ranging from 35 vol% to ϕ_{rcp} shows the microstructural difference between hard/soft particles, which affects the bulk

rheology of the system such as the viscosity or storage modulus of the system. Finally, the volume fraction regime above ϕ_{rcp} is defined as high volume fraction regime. In this paper, the system could reach up to ϕ_{rcp} using the melting and solidifying process of wax particles not only for the emulsion but also even for the suspension despite the non-deformability of hard particles themselves. High volume fraction emulsion system is solidified and the systems become suspension without loss of volume fraction or any change in droplet size.

We suggest the effect of softness of particles in micro/macroscopic system dynamics through evaluating the bulk properties of both suspension and emulsion by applying shear in a wide range of volume fraction. From this work, one could understand the behavior of suspensions in high volume fraction which has never been studied before and clarify the influence of surface softness by the comparison between emulsion and suspension.

Keywords : Emulsions, Colloids, Shape fluctuations, Wax

Student Number : 2012-20963

Contents

Abstract ..... **i**

Contents ..... **iv**

List of Figures ..... **vi**

Chapter 1. Introduction **1**

1.1. General introduction 2

1.2. Outline of the thesis 5

Chapter 2. Literature review **7**

2.1. Beyond hard particle 8

2.1.1. common features of soft particles 8

2.1.2. Comparison between emulsion and suspension 12

2.2. Micro-scale analysis using DWS 15

2.2.1. Shape fluctuation 15

2.2.2. Elasticitiy index 18

2.2.3. Scattering transport mean free path 20

Chapter 3. Experimental section **22**

3.1. Model system preparation 23

3.1.1. Materials 23

3.1.2. Preparation of crude emulsion 25

3.1.3. Refinement of crude emulsion 27

3.2. Model system characterization 29

3.2.1. System sizing 29
3.2.2. Visualization 31
3.2.3. System stability 34
3.2.4. Volume fraction of the emulsion/suspension 36
3.3. Apparatus 38
3.3.1. Diffusing wave spectroscopy (DWS) 38
3.3.2. Rotational rheometry 42
Chapter 4. Results and discussion 43
4.1. Microscale analysis 44
4.1.1. MSD for whole volume fraction regime 44
4.1.2 Diffusion coefficient under ϕ_{rcp} 46
4.1.3. Very short time behavior under ϕ_{rcp} 50
4.1.4. Elasticity index above ϕ_{rcp} 53
4.1.5. Scattering transport mean free path l^* under ϕ_{rcp} 56
4.2. Macroscale analysis 58
4.2.1. Viscosity for low/intermediate volume fraction regime 58
4.2.2. Viscoelastic behavior for high volume fraction regime 64
Chapter 5. Summary 74
Bibliography 80
국문 초록 86

List of Figures

Figure 1.1 Schematic diagram of the α-eicosene wax in water dispersed system.....3

Figure 2.1 Diagram of structural transitions in monodisperse emulsions as a function of droplet volume fraction, ϕ.....14

Figure 2.2 Schematic diagram of the photon propagation inside turbid sample and its randomized direction of light in transmission geometry. 21

Figure 3.1 (a) Image of custom-made couette cell with crude emulsion. (b) Schematic diagram of custom-made couette cell.....26

Figure 3.2 Depletion induced sedimentation/creaming process using centrifuge.....28

Figure 3.3 Number distribution of the diameter of the emulsion droplets from bright field microscopy image analysis at 30 ℃ for set A and B. 30

Figure 3.4 (a) bright-field microscopy image of emulsion. (b) bright-field microscopy image of suspension. (c) Birefringence image of suspension. 33

Figure 3.5 Cyro-SEM (PP3000T, Quorum Technologies) images of α-eicosene suspension. 33

Figure 3.6 Schematic diagram of volume fraction measurement process. ...37

Figure 3.7 Diffusing wave spectroscopy (DWS) setup. Optical configuration:

A coherent light source (Laser, Cobolt, Sweden, λ = 687 nm) is directed to the surface of a ground glass diffuser. The speckle beam created by the diffuser is collimated by a lens and then used to illuminate a sample cuvette containing the sample of interest. The scattered light is collected by a single mode fiber receiver in transmission and directed to a single photon counting module and digital correlator. 41

Figure 4.1 Apparent mean square displacement of the droplets for set A obtained from the DWS measurements at different concentrations. (a) Data taken for emulsion at T = 30 °C. (b) Data taken for suspension at T = 15 °C. 45

Figure 4.2 Onset of simple diffusive motion as diffusion regime which $\Delta < \vec{r}^2 > /6t$ is constant. 48

Figure 4.3 Non-dimensionalized diffusion coefficient D/D_0 for set A for both emulsion (red triangle) and suspension (blue inverse triangle). The black line represents the 35 vol%. 49

Figure 4.4 Analysis of the contribution of shape fluctuations to the apparent mean square displacement of the droplets at 30 °C. Solid lines are fits to the data with Eq (2.1). Inset: fitting parameters A and τ_{sf} for different droplet volume fractions. 52

Figure 4.5 Elasiticity index (EI) of the emulsions (red triangle) and suspensions (blue inverse triangle) obtained from DWS. 55

Figure 4.6 Reciprocal optical transport mean free path of the emulsions at

T=15 °C and at *T*=30 °C obtained from diffuse transmission measurements. 57

Figure 4.7 (a) Shear flow curves for the emulsion droplets at different volume fractions. The dispersion viscosity is extracted from the data over a shear rate ranging from 10 to 100 /s. (b) Shear flow curves for the suspension particles at different volume fractions. The dispersion viscosity is extracted from the data over a shear rate ranging from 6 to 60 /s. 59

Figure 4.8 (a) Viscosity of the emulsion at 30 °C as a function of the droplet volume fraction (red triangle symbols). Solid line shows the prediction for the semi-empirical expression by Lionberger&Russel. (b) Viscosity of the suspension at 15 °C as a function of the droplet volume fraction (blue inverse triangle symbols). Dashed line shows the prediction for the semi-empirical expression by Krieger&Dougherty. 60

Figure 4.9 Dynamic strain sweep test at frequency = 1 /s for 50.05 vol% sample of set A (*G'* : solid symbols, *G"* : open symbols).....63

Figure 4.10 (a) Dynamic strain sweep for 86.92 vol% sample of set B at frequency 1 rad/s. (b) Dynamic frequency sweep for 86.92 vol% sample of set B at strain 0.01 % (linear viscoelastic regime). *G'* as solid and *G"* as open symbols while emulsion is represented as red symbol and suspension is represented as blue symbol.....65

Figure 4.11 Values of storage modulus as a function of volume fraction at

frequency = 0.1, 1, 10, 100 rad/s. (a) is for the emulsion and (b) is for the suspension. 66

Figure 4.12 Values of plateau storage modulus as a function of volume fraction with emulsion as square symbol and suspension as inverse triangle symbol (unscaled). 69

Figure 4.13 Values of scaled plateau storage modulus using Laplace pressure as a function of volume fraction with emulsion as square symbol and suspension as inverse triangle symbol. Blue dotted line under ϕ_{rcp} shows power-law behavior of the suspension, $G_p' \sim \phi^3$ while blue dotted line above ϕ_{rcp} shows power-law behavior of the suspension, $G_p' \sim \phi^2$. Red dotted line follows the model equation $G_p' \sim \phi/(\phi_c - \phi)$ which diverges at ϕ_c, while red dashed line above ϕ_{rcp} follows the network-spring model $G_p' \sim \phi(\phi - \phi_c)$ 70

Figure 5.1 Structure representation for both emulsion and suspension over a wide range of volume fraction. The scheme describes how different regime of volume fraction lead to different structural response under shear and microscale diffusive motions. 76

Chapter 1.

Introduction

1.1. General introduction

Soft colloidal particles are ubiquitous in daily life and have been widely used in industry for centuries. They can be found, for example, as constituents of mayonnaise, lotions, thickeners, or drilling fluids. For this variety of industrial applications, many researches have been done to probe the Brownian thermal motion and rheological properties of emulsion such as its behavior under shear flow or yield stress of emulsion in high volume fraction.[1–3] Typical hard particle suspension system was not reachable to the high volume fraction regime above ϕ_{rcp} due to its non-deformability of particle itself.

We set out to design and study the thermal motion and the rheological properties of a tunable model systems based on emulsified wax with properties that can be tuned from liquid to solid. We use α-eicosene wax suspension system as a model system to achieve highly concentrated particle systems like the emulsion. One can easily change the softness of a single particle which can affect the mechanical properties of model system by changing the temperature as summarized in Figure 1.1. At low temperature below T_c (melting point 24.6 ℃), the system can be categorized as a suspension because the wax solidifies and the particle has hard surface. At high temperature above T_c, wax is liquefied and the surface becomes soft, so

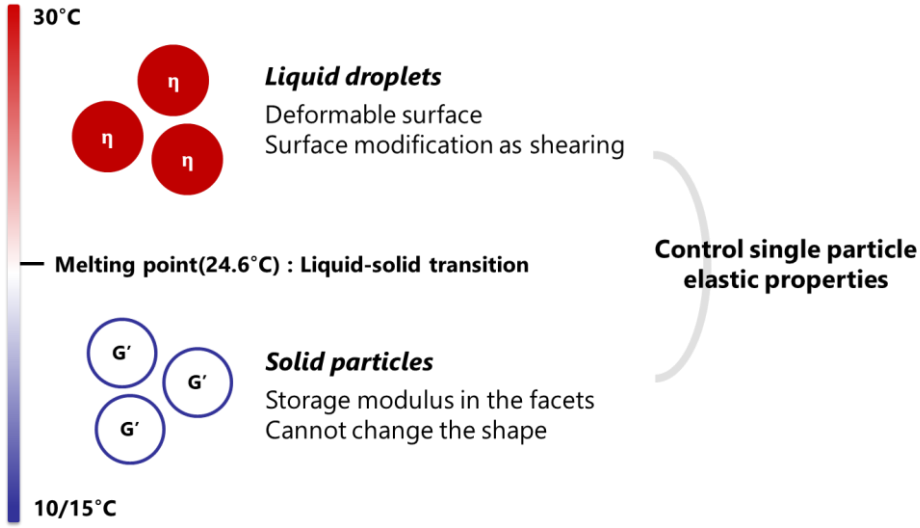

Figure 1.1 Schematic diagram of the α-eicosene wax in water dispersed system.

that the system is considered as an emulsion. The transition allows us to control the single particle elastic properties, which affects thermal fluctuations of the droplet interface and finally mechanical properties of the bulk system.

Here we compare the hard particle suspension and soft particle emulsion system and then take a look at the systems' dynamics under and above ϕ_{rcp}, for monodisperse suspension~0.64) using DWS and rheometer. By the comparison we could estimate the physical properties of the high volume fraction suspension system for the micron-sized colloidal system and also suggest the system's internal structure which has not been previously studied for highly concentrated system.

1.2. Outline of the thesis

The thesis is organized into introduction, literature review, experimental methods, and several results on the dynamics of wax-in-water system over a wide range of volume fraction and ends with a conclusion.

In Chapter 2, the basic background of the thesis will be described. It is divided into the characteristic of soft particles and the techniques of analyzing the microscale DWS data. The first part of Chapter 2 describes common features of soft particles and especially focuses on the difference between hard particle suspension and soft droplet emulsion. The second part of Chapter 2 explains shape fluctuation, elasticity index, and scattering transport mean free path and this background knowledge is used to analyze the mean square displacement data in Chapter 4.1.

In Chapter 3, preparation and characterization of the α-eicosene system and the experimental methods are described. Several methods, such as Cryo-SEM and bright field microscopy, are used to visualize the droplets' shape and facets of the interface. Basic properties, such as viscosity of pure wax or the measurement of volume fraction, are also explained in detail.

In Chapter 4, there are the main results on the α-eicosene wax dispersion for micro and macro scale using DWS and rheometer. In Chapter 4.1., the data from the DWS is investigated: for the low and intermediate volume fraction

regime, the data clearly shows the effect of softness on the diffusion coefficient and shape fluctuation. For high volume fraction regime, elasticity index becomes important parameter to indicate the softness of particle. In Chapter 4.2., the viscosity and the plateau storage modulus are characterized to describe the elasticity of the system. Plateau storage modulus have size dependence for almost whole volume fraction regime except high volume fraction regime of suspension. This implies the different origin of elasticity affects to the size dependence of the bulk scale elasticity of particulate system.

Chapter 5 will close the thesis with a brief conclusion that summarizes the main result. In this Chapter, a few suggestions are made which need to be considered for future work.

Chapter 2.

Literature review

2.1. Beyond hard particle

2.1.1. Common features of soft particles

In experiments, one can distinguish three typical cases of soft particle systems. On the soft side one can find highly deformable particles with a fuzzy interface such as microgels or weakly screened charged particles with long range repulsive interactions. [4–6] On the stiff side, and in the limit of negligible compression or deformability, the case of hard spheres is approached. In an experiment the hard sphere limit can be realized, to within a good approximation, by preparing sterically stabilized solid particles such as PMMA spheres used in many studies. [7–9]

A plethora of theoretical and fundamental experimental work has been dedicated to this idealized case. Moreover, many dispersion properties can be mapped on this simplified case by introducing an effective volume fraction taking account for finite ranged repulsive interactions. [10] Dispersions made from repulsive particles have been studied widely and under a variety of different conditions and in mixtures. [11]

What has been lacking until now are studies on a particle model system with a sharp interface where the properties of the particles could be tuned in situ from deformable to hard without leading to aggregation. The sharp interface

is of key importance for a clear definition of the volume fraction and the random close packing or jamming condition. [12] Equally, in computer simulations of soft spheres the interactions are usually modeled by a harmonic or anharmonic repulsive interaction potential with a sharp onset upon contact. [13,14]

Tunable model systems such as microgels, however, generally feature rather fuzzy interfaces which makes it difficult to pinpoint the condition for marginal particle–particle contacts – also known as the isostatic condition – where a percolated network of contacts can bear a finite load. The latter is a hallmark of the athermal jamming condition. [13–16] Emulsion droplets are probably the closest model system for such deformable but elastic colloidal objects that possess a sharp, nanoscale liquid-liquid interface. [2,14]

Since suspensions have been studied for a long time, it will be useful to compare the characteristics of emulsions that can be physically differentiated from those of suspensions. Thus, the existing theories based on the suspension system can be used to analyze the micro/macroscopic dynamics of the emulsions, such as Krieger&Dougherty equation. [17]

But this is not always possible due to the two main limits of the system, which makes direct comparison between emulsion and suspension impossible. First of all, one could not perfectly control the variables when comparing the systems. In many researches comparing emulsion and suspension, it is

common to use a monodisperse polystyrene in water system as a model suspension, and silicone oil-in-water system for the model emulsion. The basic physical properties of two model systems such as density, refractive index, interfacial tension, etc., are not the same and one should distinguish whether the differences in rheological properties come from basic physical differences or softness of the particles, which is impossible with these kinds of model systems. The investigated volume fraction regime is also limited to under random close packing (RCP) volume fraction. Although emulsion could easily reach higher volume fraction regime well above ϕ_{rcp} by its unique soft and adjustable interface in high shear/stress condition, the volume fraction regime of hard particle suspension is normally limited to under ϕ_{rcp} due to its hardness of the surface. Therefore, previous researches dealing with high volume fractions above ϕ_{rcp} focus on the pure characteristics of the emulsion without comparison to the hard sphere suspension system. In fact, emulsion is thermodynamically unstable and tri-component system including interfacial stabilizer, such as surfactant, and such characteristic makes the situation more complicated for the analysis.

To overcome two mains limits indicated above, we use α-eicosene wax dispersed in water system which has melting point at 24.6 ℃. This system changes its characteristic from suspension to emulsion or vice versa by just changing the temperature. Above the melting point, wax melts and the

particles become soft, while below the melting point, wax solidifies and becomes hard. By just changing the temperature, we could overcome the first limit mentioned above: the basic properties of the particles except the softness are the same, so the other physical properties of the particles do not play a significant role to the bulk mechanical properties of the system. For the case of second limit, we expand the work to the wide range of volume fraction.

2.1.2. Comparison between emulsion and suspension

The remarkable features of soft particle systems can be related directly to their interfacial deformability. Since soft particles dissipate stress by compression or by deforming their interface upon shear, systems can be prepared at higher volume fraction ϕ than imposed by the random close packing limit of hard spheres $\phi_{rcp} \simeq 0.64$ as shown in Figure 2.1. [1–4,18,19]

Due to the deformability of soft particles, the emulsion easily reaches high volume fraction regime and then the particle is solidified to become hard particle suspension. In this regime, the particles have deformed shape with facets at the interface and the images of such facets are clearly captured for Pickering emulsion. [20] In the limit of very high volume fraction, the system shows a foam-like structure [21,22] which consists of a network of thin films of continuum phase, and the mechanical stability of system is determined entirely by the strength of the thin film at the plateau borders. [22]

Since the emulsion and suspension are based on the different particle surface softness, the origin of elasticity of these two systems are also different. For the suspension under ϕ_{rcp}, the origin is suggested as the Brownian forces [23] while the elasticity for the emulsion under ϕ_{rcp} comes from thermal fluctuations. [1] Above ϕ_{rcp}, the elasticity comes from the compressed

repulsive droplets by an external osmotic pressure, and finally permits the storage of interfacial elastic energy. [24] The droplets start to be distorted by the presence of the neighboring particles and this additional deformation results in the elasticity of the emulsion. However, the origin of elasticity of the suspension in this high volume fraction regime is not yet known since this regime has never been explored.

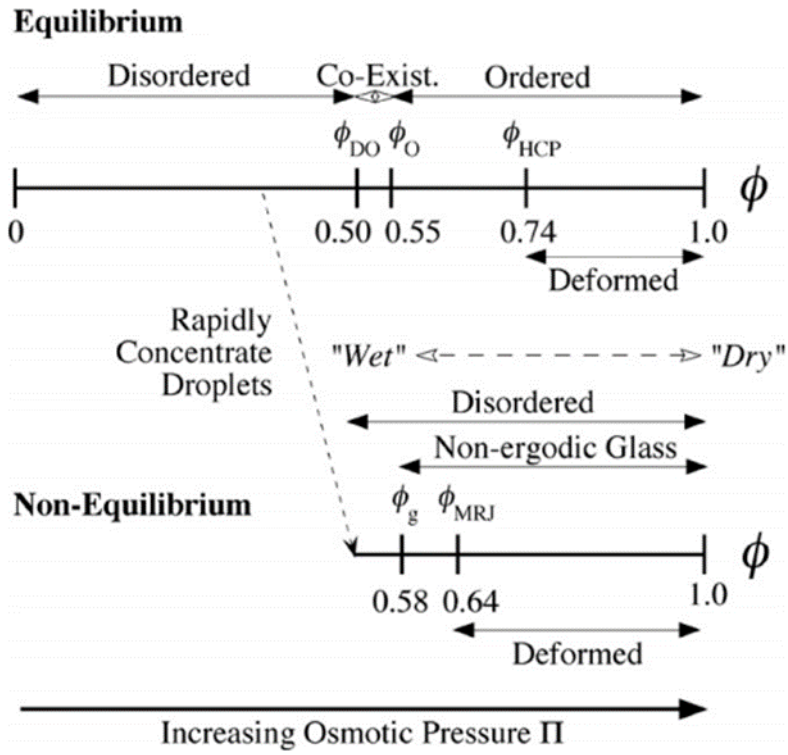

Figure 2.1 Diagram of structural transitions in monodisperse emulsions as a function of droplet volume fraction, ϕ.

2.2. Micro-scale analysis using DWS

2.2.1. Shape fluctuation

For hard colloidal particles in low viscosity Newtonian solvents, such as water at ambient temperatures, contributions to the inertia of the particle and the displaced fluid lead to non-diffusive motion at short times. The principles of thermal Brownian motion can be understood in terms of a simple Langevin equation $m\frac{\partial^2\vec{r}(t)}{\partial t^2} + 6\pi\eta R\frac{\partial\vec{r}(t)}{\partial t} = \overrightarrow{F_{th}}(t)$ where m is the inertial mass of the particle, $\overrightarrow{F_{fr}}(t) = 6\pi\eta R\frac{\partial\vec{r}(t)}{\partial t}$ is the Stokes friction force and $\overrightarrow{F_{th}}(t)$ is the force arising from random thermal fluctuations.

For a particle at long times $t \to \infty$ the motion is diffusive with $\langle \Delta r^2(t)\rangle = 6Dt$. For extremely short times the motion becomes ballistic with $\langle \Delta r^2(t)\rangle \propto t^2$. At intermediate times the time evolution depends on the details of the interaction between the particle and its surrounding fluid. In a simplified picture of Brownian motion, the friction force acts instantaneously on a change of the particles velocity. However, when the particle receives momentum, it displaces the fluid in its immediate vicinity. The surrounding flow field is altered and acts back on the particle due to a non-negligible fluid inertia, as first described quantitatively by Hinch. [25,26] The friction force then includes additional terms that depend on the particles past motion, which

leads to a hydrodynamic memory effect and a corrected form of the Langevin approach. [27] Such a hydrodynamic effect delays the transition from ballistic to diffusive motion, resulting in a persistence of the non-diffusive motion to much longer times. [25]

At short times, shape fluctuations are a competing mechanism that can lead to thermally excited motion and they are a consequence of the deformability of the particles' interfaces and of the viscosity of the dispersed fluid. Fluctuations at an interface between a fluid and the solvent can be induced thermally as capillary waves. The amplitude of the wave is determined by deformability given by the surface tension of the droplet. The damping scales with the fluid viscosity. Interfacial motion can thus be thermally excited leading to shape fluctuations of the droplets on the nanoscale. [28] The standard DWS formalism does not consider shape fluctuations and here the additional motion simply shows up as an apparent increase of displacement at short times. This additional contribution can be included as follows:

$$\langle \Delta \vec{r}_{app}^{\,2}(t) \rangle = \langle \Delta \vec{r}^{\,2}(t) \rangle + \frac{3}{k_0^2(1-g)} \left[\frac{\Delta\sigma(0) - \Delta\sigma(t)}{\sigma_0} \right] = \langle \Delta \vec{r}^{\,2}(t) \rangle + f(t) \qquad (2.1)$$

where $g = 1 - l_s/l^*$ denotes the scattering anisotropy parameter (i.e. the mean of the cosine of the scattering angle [29]) and l_s is the scattering mean free path. The magnitude and relaxation of the droplet shape fluctuations are

described by the function $f(t) \propto \{\Delta\sigma(0) - \Delta\sigma(t)\}/\sigma_0$. $\Delta\sigma(t)$ decays to zero and the entire function $f(t)$ plateaus after a characteristic relaxation time, in contrast to the center of mass displacement which is unbounded for a liquid emulsion. Therefore, the center of mass displacement dominates at long times. Whether the shape fluctuations are picked up by DWS or masked by the center of mass diffusion now depends on the magnitude of $f(t)$ and the relaxation time. A full theoretical analysis of the different contribution of the spectrum of excited modes to the shape fluctuations is reported in the work of Gang and coworkers. [28] For simplicity we only consider the principal relaxation mode $\Delta\sigma(t)/\Delta\sigma(0) = \exp(-t/\tau_{sf})$ with a relaxation time of the dominant mode τ_{sf}. We can then express the contribution of the shape fluctuations to the apparent MSD as Eq (2.2) :

$$f(t) = \frac{3}{k_0^2(1-g)}\left[\frac{\Delta\sigma(0)-\Delta\sigma(t)}{\sigma_0}\right] \simeq A[1 - \exp(-t/\tau_{sf})] \qquad (2.2)$$

In the dilute limit, the amplitude of the fluctuations $A = 3\Delta\sigma(0)/\sigma_0 k_0^2(1-g)$ is predicted to scale inversely with the surface tension Γ and the relaxation time τ_{sf} is proportional to the viscosity of the dispersed phase η_{wax} in the limit $\eta_{wax} \gg \eta$.

2.2.2. Elasticitiy index

For the particulate system, any given particle is temporarily confined to a cage of nearest neighbors. If the concentration is not high enough(under ϕ_{rcp}), the movement of particles can be slow down for short time scale but can finally escape from its cage by diffusive motion. Meanwhile the concentration increases above ϕ_{rcp}, not only the short time motion but the long time scale diffusive motion escaping from the cage of the particles essentially vanishes and particles become permanently trapped in their cages. The motion of concentrated system is limited to the short length self-diffusion within the cages and long time scale dynamics shows highly correlated dynamics which may stop eventually. [30]

The dynamics of the system reflected in different ways in MSD data depending on its volume fraction. As the concentration increases, the movement of a single particle changes as time increases: the diffusion slows down which is reflected as a decrease in slope for the short time scale, while the MSD reaches to the plateau value which manifests the solid-like character of the sample due to the restricted motion by other surrounding particles for the long time scale. This plateau reflects the elasticity of the system. As the plateau is lower, the network becomes tighter and the elasticity is stronger. [31] Elasticity index can be defined as in Eq (2.3) [31] to quantitatively

analyze the systems' elasticity in passive micro-rheological approach.

$$\text{EI (Elasticity index)} = 1/\text{ (plateau height of MSD)} \qquad (2.3)$$

Compared to the elastic modulus in bulk rheology which can be measured for whole volume fraction regime, EI can only be achieved in high volume fraction regime because the particle movement is only caged above ϕ_{rcp}.

2.2.3. Scattering transport mean free path

The scattering transport mean free path, l^* is a measure of the light scattering strength or optical density. The scattering transport mean free path is defined as the average length which the direction of propagation of the photon in a strongly diffusing medium is randomized. It is related to the mean free path of a moving particle inside the medium. The schematic diagram for scattering transport mean free path is in Figure 2.2.

For the roughly spherical objects studied here we can attempt to model l^* based on Mie scattering theory taking into account positional correlations via the well-known Percus&Yevick structure factor $S(q)$. [32] The latter has been shown previously to be a good model to describe the scattering from liquid emulsions below the jamming point $\phi \leq 0.6$. [33]

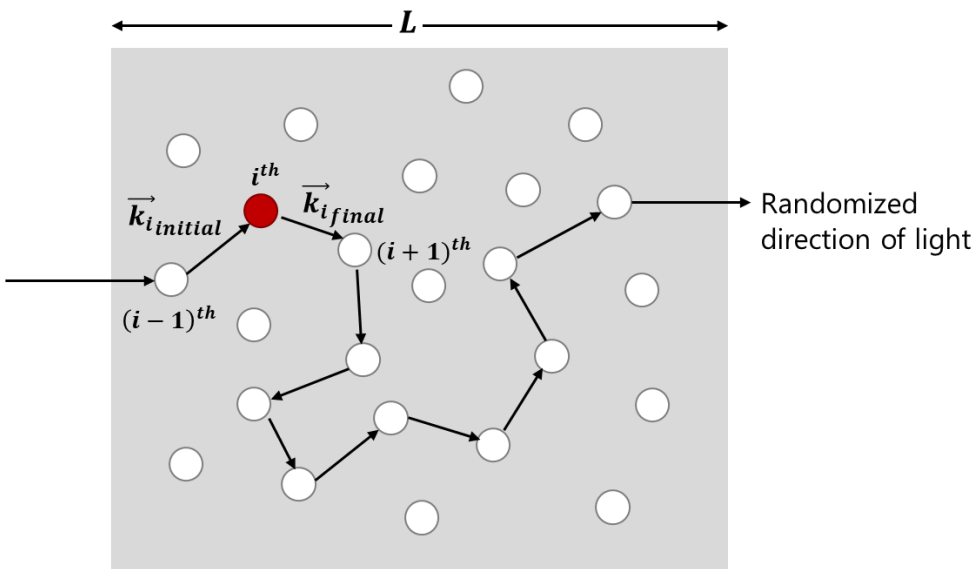

Figure 2.2 Schematic diagram of the photon propagation inside turbid sample and its randomized direction of light in transmission geometry.

Chapter 3.

Experimental section

3.1. Model system preparation

3.1.1. Materials

We study α-eicosene-in-water emulsions stabilized by 10 mM sodium dodecylsulfate (SDS > 90%, from Sigma–Aldrich). α-eicosene wax (1-eicosene, $CH_3(CH_2)_{17}CH = CH_2$, Sigma–Aldrich, technical grade, purity >80%) is chosen as the dispersed phase because in the bulk it solidifies at temperatures below melting point. The melting point T_c specified by the manufacturer is 24~30 ℃ and we have performed temperature sweeps from 50 ℃ to 10 ℃ in order to determine the exact melting point with a commercial rheometer. In temperature sweeps, the viscosity η_{wax} increases sharply below 24.6 ℃ indicating the liquid-solid transition is located around 24.6 ℃.

We determine the density of α-eicosene in house to $\rho_{wax} = 0.8\ \mathrm{g/cm^3}$, in agreement with literature specifications for the pure substance $\rho_{wax} = 0.79\ \mathrm{g/cm^3}$. [34] Within the limited resolution of our volumetric measurements, we do not observe a significant temperature dependence of ρ_{wax} over the range 50~10 ℃ studied. The value for the refractive index $n = 1.44$ is taken from the literature. [34]

To access the viscosity in the liquid phase of our batch we measure the zero

shear viscosity, η_{wax} with a commercial rheometer (MCR502, Anton Paar, Austria). We find $\eta_{wax} = 4$ cP for T = 30 ℃ compared to the viscosity of water $\eta_{wax} = 0.8$ cP at the same temperature.

3.1.2. Preparation of crude emulsion

The preparation of crude emulsion is based on a procedure initially reported in. [35] Oil droplets are prepared above 50 ℃ by shear rupturing of a crude emulsion in a custom-made couette cell. [36] The schematic diagram of custom-made couette cell is presented in Figure 3.1. High speed (3,000 rpm) motor is used to grind the sample with high shear rate and the cell has 0.5 mm gap with one coarse grained interior face. In the crude emulsion, droplets have wide range of size distribution from few nm to several mm. We note that uniform discotic wax particles can also be produced via electrospray emulsification. [37]

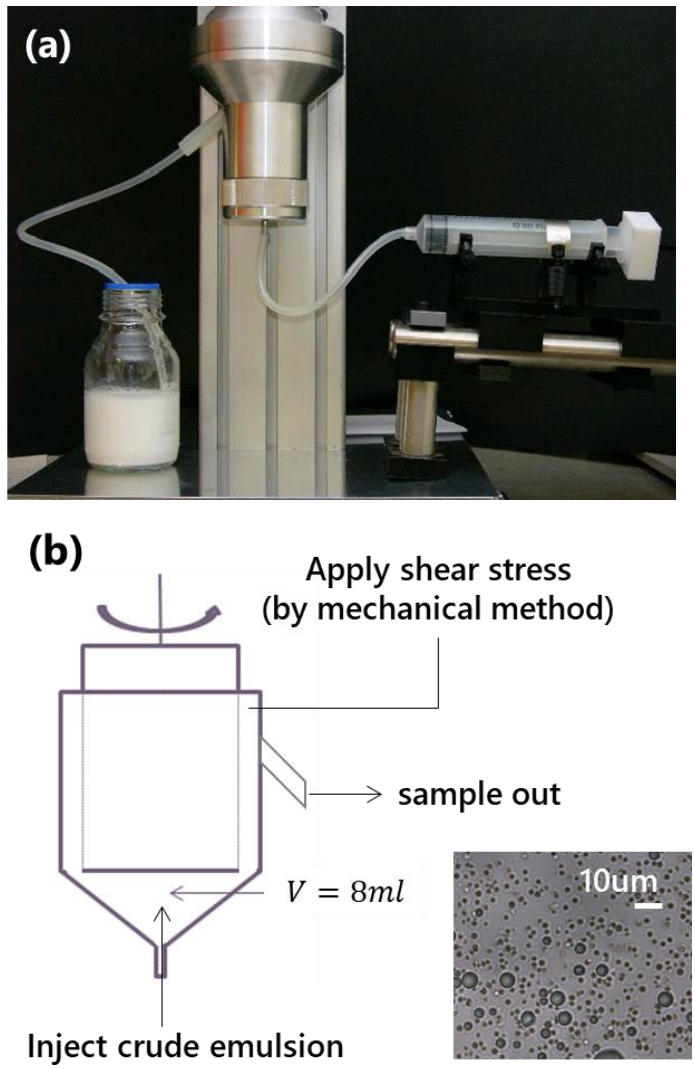

Figure 3.1 (a) Image of custom-made couette cell with crude emulsion. (b) Schematic diagram of custom-made couette cell.

3.1.3. Refinement of crude emulsion

Centrifuge is used to reduce the polydispersity of crude emulsion from 3.1.2. and to change the surfactant from NP7 to SDS. Subsequent size fractionation using depletion induced sedimentation/creaming method [35,38] results the polydispersity of the sample is successfully reduced to 25 % as in 3.2.1. The supernatant fluid after each centrifugation is exchanged to SDS 10 mM solution for exchanging surfactant. Final yield of emulsion is around 20 % and the total process is briefly illustrated in Figure 3.2.

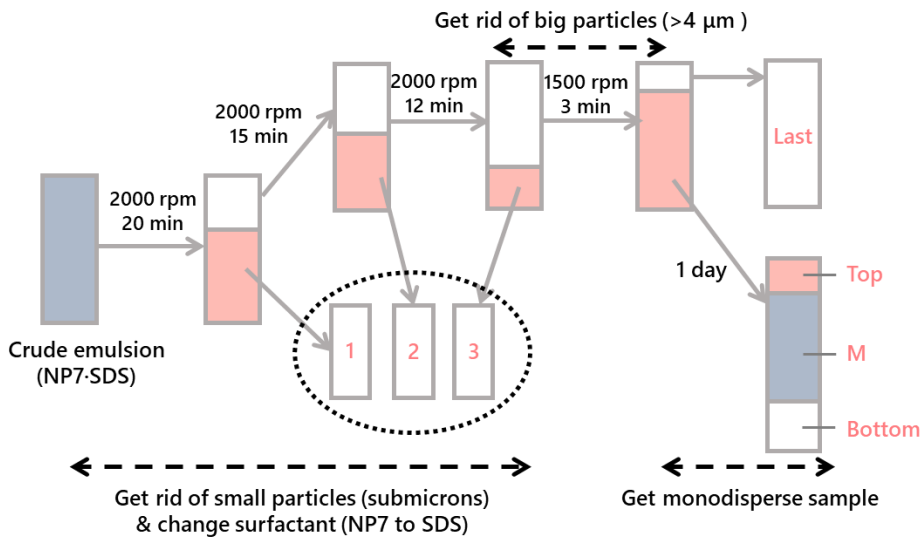

Figure 3.2 Depletion induced sedimentation/creaming process using centrifuge.

3.2. Model system characterization

3.2.1. System sizing

The size distribution is derived from bright field microscopy via particle imaging analysis, as shown in the Figure 3.3. Two sets of samples with different average diameter and polydispersity were obtained: named as set A and B. Around 400 particles were used to get reliable data. Set A is defined with average diameter of 3.52 um, polydispersity (standard deviation/average diameter) of 25.6 % and the volume fraction ranging from 10.69 to 90.17 vol%. Meanwhile set B has average diameter of 1.75 um, polydispersity of 13.1 % and volume fraction ranging from 30.49 to 82.00 vol%. Given the significant polydispersity, crystallization of the particles is suppressed.

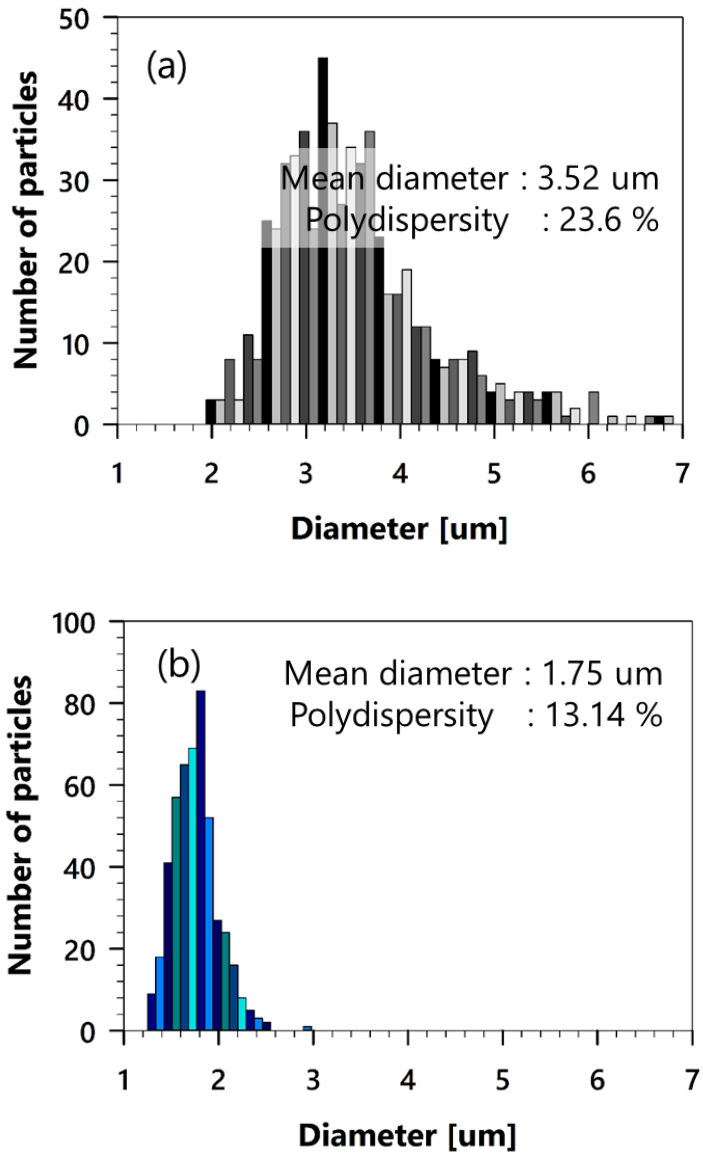

Figure 3.3 Number distribution of the diameter of the emulsion droplets from bright field microscopy image analysis at 30 ℃ for set A and B.

3.2.2. Visualization

By visual inspection using microscopy we can readily observe that the droplets turn into solid wax particles, Figure 3.5. We can also observe that the solidification can induce a shape change of the particles and these shape changes were already reported in. [35] In Figure 3.5(b), some of the solidified droplets acquire a non-spherical shape during the solidification of the α-eicosene while the emulsion is composed of spherical droplets as in Figure 3.5(a).

To clarify the existence of facets in interfaces, particles at very low temperature were observed using Cryo-SEM, Figure 3.5. α-eicosene dispersion was fast frozen plunging them into liquid nitrogen and then fractured cross-sectionally. The facets are clearly shown in all magnification.

The formation of faceted and disc like shapes can be explained by the fact that the liquid to solid phase transition is most likely liquid to a smectic-like rotator phase of a liquid crystal. [35] These disc-like particles are then optically anisotropic, exhibiting interesting light–dark birefringence while rotationally and translationally diffusing in cross-polarized light [35] in Figure 3.5(c).

In general, this means that for T = 30 ℃, above the transition temperature, the liquid α-eicosene droplets retain a nearly spherical shape while for T = 10

or 15 ℃, below the transition temperature, the solid α-eicosene particle have a distorted shape.

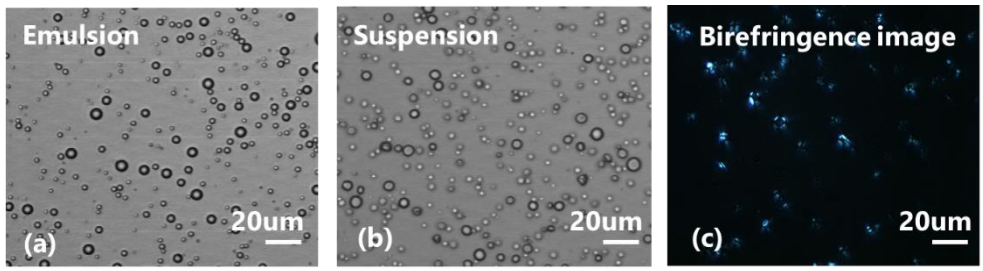

Figure 3.5 (a) bright-field microscopy image of emulsion. (b) bright-field microscopy image of suspension. (c) Birefringence image of suspension.

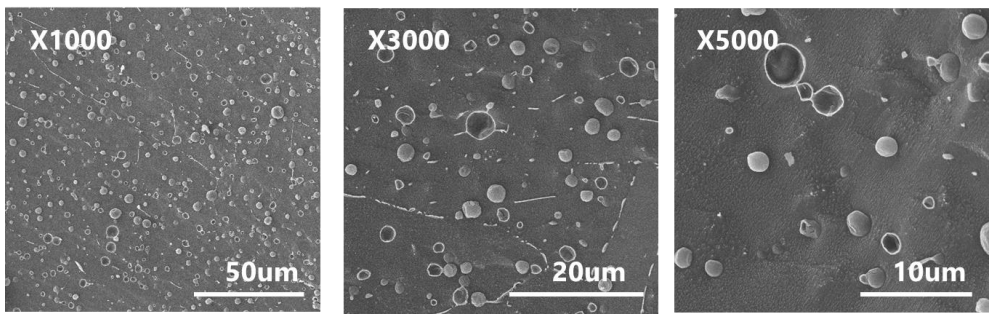

Figure 3.5 Cyro-SEM (PP3000T, Quorum Technologies) images of α-eicosene suspension.

3.2.3. System stability

We monitor the emulsions repeatedly over time by microscopy and find them to be stable for several days up to weeks but observe signs of droplet coalescence after about 8 weeks. Experiments were done in 1 month after prepared to ensure that the stability of the sample does not vary significantly. Emulsions were stored in an oven well above melting point at around 40 ℃ at an approximate volume fraction of 40 vol%. Drying was prevented by careful sealing.

Below the melting point (24.6 ℃), the α-eicosene has turned into solid wax and the particle shape slowly evolves over many hours to days, becoming less spherical and even exhibiting facets. The transition time of solidification depends on the final temperature of the sample. At 20 ℃, the transition of emulsion to suspension takes over 10 hrs which is too long to avoid drying effect, but it can be reduced to under 3 hrs at 15 ℃ or 10 ℃. In order to induce a sharp and sufficiently fast transition, we take measurements at 10/15 ℃, well below the bulk melting transition temperature to avoid the influence of possible droplet size effects on the melting temperature T_c and to make sure that the solid α-eicosene phase is rapidly reached. This way we can also exclude that the wax in some of the droplets could remain trapped in a supercooled liquid state for an extended period of time. Above the melting

point, the samples were stabilized at 30 ℃ for the entire range of volume fraction.

To make sure that there are no size changes of droplets, which could be caused by coalescence due to strong shear, etc., we compared the viscosity and storage modulus of the sample at emulsion sate and it shows no temperature history dependency over 10 repeated cycles of suspension – emulsion – suspension transition.

Moreover, the stabilization of the α-eicosene by the SDS surfactant layer at the liquid-liquid interface is likely not retained in the same way as in the liquid state of α-eicosene-in-water. Nonetheless, as we will show later in the text, we find stable dispersions and the Brownian motion probed by DWS shows no signature of aggregation or phase separation. Although the SDS concentration is slightly above the critical micelle concentration (CMC) around 8 mM, any residual micelle-induced depletion attractions between droplets are weak compared to k_BT. No phase inversion occurs even for the highly concentrated emulsion case.

3.2.4. Volume fraction of the emulsion/suspension

The α-eicosene weight fraction of a concentrated stock emulsion is determined by drying and weighing a sufficient amount of sample and from this we can determine the droplet volume fraction from the known densities of α-eicosene and water. The density ratio of α-eicosene/water is 0.792 in literature specification. The volatility of wax is also considered and the whole process for getting weight fraction of emulsion is summarized in Figure 3.6. By using Eq (3.1), we can convert the weight fraction to volume fraction.

$$\text{vol\%} = 100/\{1 + 0.792 \times ({}^{100}/_{\text{wt \%}} - 1)\} \qquad (3.1)$$

The resulting volume fraction covers wide range of volume fraction from 10 to 90 vol% which covers almost entire volume fraction regime.

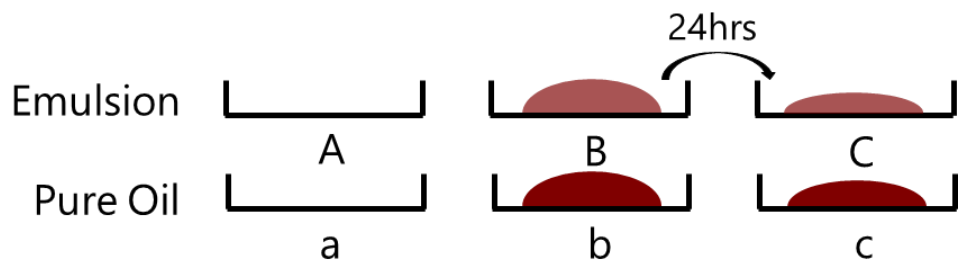

$$\text{wt\%} = \{(C - A)/(B - A)\} \times \{(b - a)/(c - a)\} \times 100$$

Figure 3.6 Schematic diagram of volume fraction measurement process.

3.3. Apparatus

3.3.1. Diffusing wave spectroscopy (DWS)

To gain access to the internal dynamic properties of our dense emulsion systems we use diffusing wave spectroscopy (DWS) in multiple scattering condition due to high turbidity of the system. DWS is a modern light scattering technique that probes the motion of particles in turbid colloidal media. The method is based on the analysis of the fluctuations of coherent laser light scattered multiple times within a sample. DWS is very similar to conventional dynamic light scattering (DLS). Both entail the measurement of a temporal fluctuations in single speckle spot of the scattered light and these fluctuations are analyzed by their temporal autocorrelation function which reflects the dynamics of the scattering medium. However, unlike DLS, DWS assumes numerous scattering events inside the sample so the light pass becomes random which implicates that the dynamics of the system could be understood in the base of statistical approximation.

In the calculation of temporal autocorrelation function in DWS, two fundamental approximations exist. The first approximation is about the light propagation. In the limit of very high multiple scattering, the light path of each photon could be described as a random walk. This simple description is

also known as diffusion approximation, and this includes that the any interference is neglected. The second approximation assumes that every single individual scattering events are approximated by the contribution of an averaged scattering event. Since there are numerous scattering events playing a less critical role, the path length of the light obtained using the diffusion approximation above determines the number of the average scattering events.

Through these two approximation, intensity-intensity correlation function could be analyzed to gain additional information for the systems' internal dynamics. Given the large size of the droplets we predominantly probe self-motion and shape fluctuations [28,39–41] while the contribution of collective motion to the dynamic multiple light scattering signal can be neglected. We can then express the measured and normalized intensity–intensity correlation function $\mathrm{g}_2(t)$ as follows [40–42] :

$$g_1(t) = \sqrt{g_2 - 1} = \frac{(\frac{L}{l^*}+\frac{4}{3})\sqrt{k_0^2\langle\Delta r^2(t)\rangle}}{\sinh\{(\frac{L}{l^*}+\frac{4}{3})\sqrt{k_0^2\langle\Delta r^2(t)\rangle}\}} \tag{3.2}$$

Here $k_0 = 2\pi n/\lambda$ denotes the wavenumber of light, λ is the laser wave length, n is the refractive index of the continuous phase, l^* is the optical transport mean free path, L is the cuvette path length and $\langle\Delta r^2(t)\rangle$ is the apparent average particle mean square displacement (MSD). The measured photon count rate is proportional to the total transmission coefficient for

diffusely scattered light T, which in turn is given by $T \propto l^*/L$. In the experiment $\langle \Delta r^2(t) \rangle$ is extracted directly from the correlation function using the instrument software. By calibration, using a sample with a known value of l^*, we also gain access to the so-called transport mean free path of light of the samples at the wavelength of the laser employed, $\lambda = 687$ nm. [40]

The intensity–intensity correlation function is recorded with a commercial DWS instrument (DWS RheoLab, LS Instruments AG, Switzerland) and the schematic diagram for DWS is represented in Figure 3.7. The gap of the cell is varied from 0.5 mm to 5 mm which is determined by sample's transport mean free path l^* and the concentration. From the light scattering experiment, we can extract the MSD data and capture the particle movement changes in long time scale as the temperature changes.

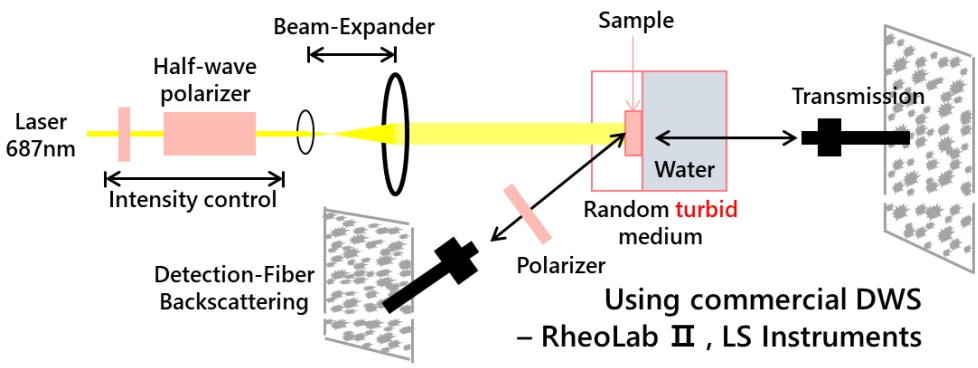

Figure 3.7 Diffusing wave spectroscopy (DWS) setup. Optical configuration: A coherent light source (Laser, Cobolt, Sweden, λ = 687 nm) is directed to the surface of a ground glass diffuser. The speckle beam created by the diffuser is collimated by a lens and then used to illuminate a sample cuvette containing the sample of interest. The scattered light is collected by a single mode fiber receiver in transmission and directed to a single photon counting module and digital correlator.

3.3.2. Rotational rheometry

Macroscopic mechanical properties of set A and B were measured using stress-controlled type rheometer (MCR300 from Anton Paar Physica). Solvent trap was equipped to prevent drying and evaporation. 50mm cone and plate geometry is used for fine measurement of the sample.

Before the measurement, preshear at 100 /s for 60 s and rest for 300 s is applied and the effect of loading is removed for all experiments. The emulsion at high temperature under ϕ_{rcp} shows a Newtonian behavior. For high volume fraction of both emulsion and suspension systems, we analyze the behavior of both suspension and emulsion systems under small amplitude oscillatory shear. Strain sweep test is done at frequency = 1 rad/s and the strain range of 0.001 ~ 100 %. The frequency sweep test is also done in the range of strain where linear viscoelasticity is guaranteed (0.01 to 1 % in the experimental concentration regime).

Chapter 4.

Results and discussion

4.1. Microscale analysis

4.1.1. MSD for whole volume fraction regime

We study the thermal motion of the particles center of mass and fluctuations of the liquid interfaces using DWS for whole volume fraction regime for set A in Figure 4.1. As mentioned in 2.2, apparent mean square displacement of the particles could be analyzed in following ways: at intermediate time scale around t~ms, one can expect the apparent MSD to show simple center of mass diffusion $\langle \Delta r^2(t) \rangle = 6D(\phi)t$. At short time scale around t ~ ns, however, we observe strong deviation from the constant value with clear differences indicating the effect of softness in 4.1.3. At long time scale above ϕ_{rcp}, we do indeed observe the onset of elasticity as the plateau value of MSD while the dispersion is liquid and no plateau exist for the system under ϕ_{rcp}. The detail information from Figure 4.1 will be analyzed in the following chapters and this section ends up with the analysis of the scattering transport mean free path, l^* which reflects the droplets' refractive index and surface properties in 4.1.5.

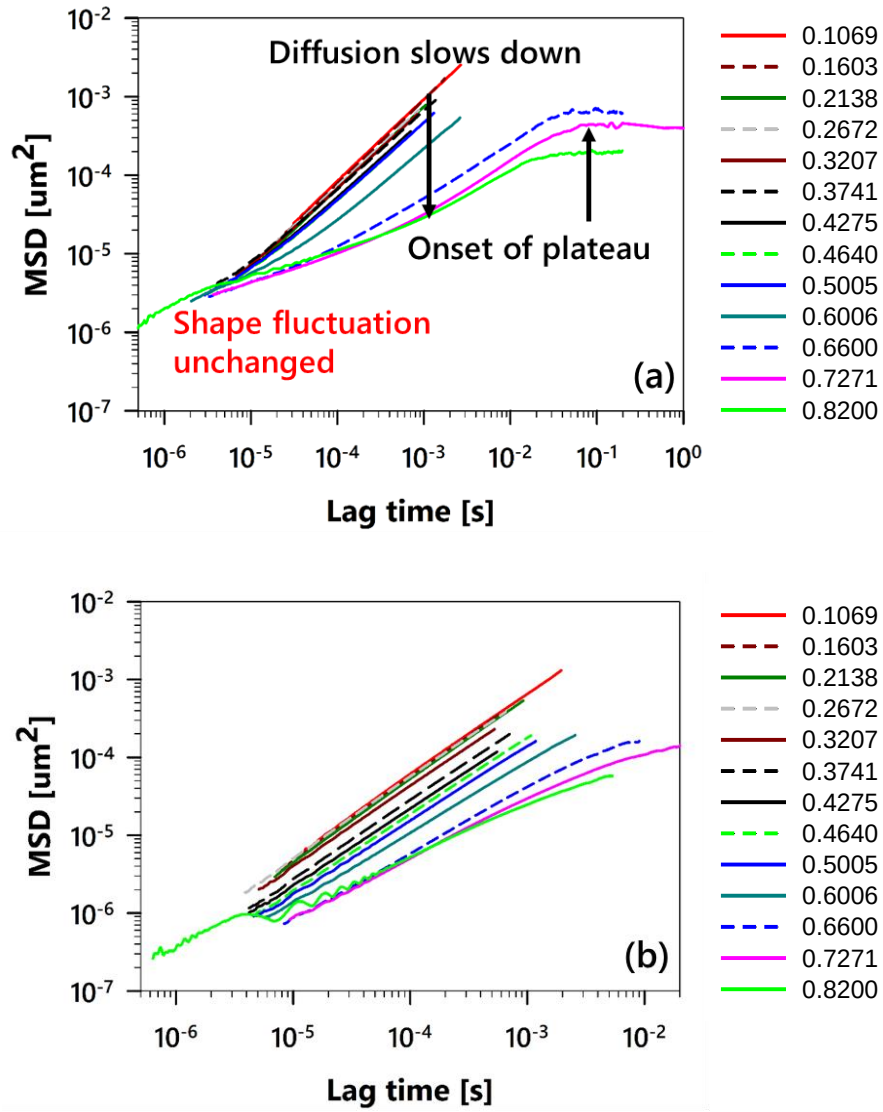

Figure 4.1 Apparent mean square displacement of the droplets for set A obtained from the DWS measurements at different concentrations. (a) Data taken for emulsion at T = 30 °C. (b) Data taken for suspension at T = 15 °C.

4.1.2 Diffusion coefficient under ϕ_{rcp}

Now we focus our attention on the short time diffusion coefficient $D(\phi)$ obtained from the DWS experiments. To be able to identify the onset of simple center of mass diffusion regime, we plot $\langle \Delta r^2(t) \rangle / 6t$ in Figure 4.2 and thus in the diffusive regime $\langle \Delta r^2(t) \rangle / 6t$ is constant. In Figure 4.3, we show the results for the two different temperature studied and the concentration dependence of the $D(\phi)$ extracting from the plateau over the time range 10^{-4} s ~ 10^{-3} s. $D(\phi)$ is demonstrated in Figure 4.3 to see the effect of surface softness on the microscopic behavior of the system. To compensate the effect of temperature on diffusion coefficient, $D(\phi)$ is non-dimensionalized as $D(\phi)/D_0$ using the coefficient for unhindered free diffusion as $D_0 = \frac{k_B T}{6\pi\eta R}$ by Stokes-Einstein relation thereby taking into account the fact that the diffusion scales with the temperature.

As expected, the short time self-diffusion constant $D(\phi)$ decreases as the dispersion becomes more crowded. At low volume fraction regime, emulsion and suspension do not show a big difference in D. The collapse of the two data sets shows that the deformability of the interface has relatively little impact on the center-of-mass diffusion. However, above 35 vol%, which we will define as intermediate volume fraction regime, hard particle suspension system clearly deviates from soft particle emulsion. 35 vol% becomes

criterion which reflects sudden slope change of suspensions' diffusion coefficient. By Figure 4.3, low and intermediate volume fraction can be defined: low volume fraction regime under 35 vol%, intermediate volume fraction regime above 35 vol% to ϕ_{rcp}.

The dramatic decrease of $D(\phi)/D_0$ at 35 vol% for hard particle suspension indicates the diffusive motion of a single particle begins to be limited by the presence of other particles even though the particles are not necessarily in touch with each other. The confined diffusive motion of hard particles can be explained by the change of interparticle potential caused by the change of surface softness.

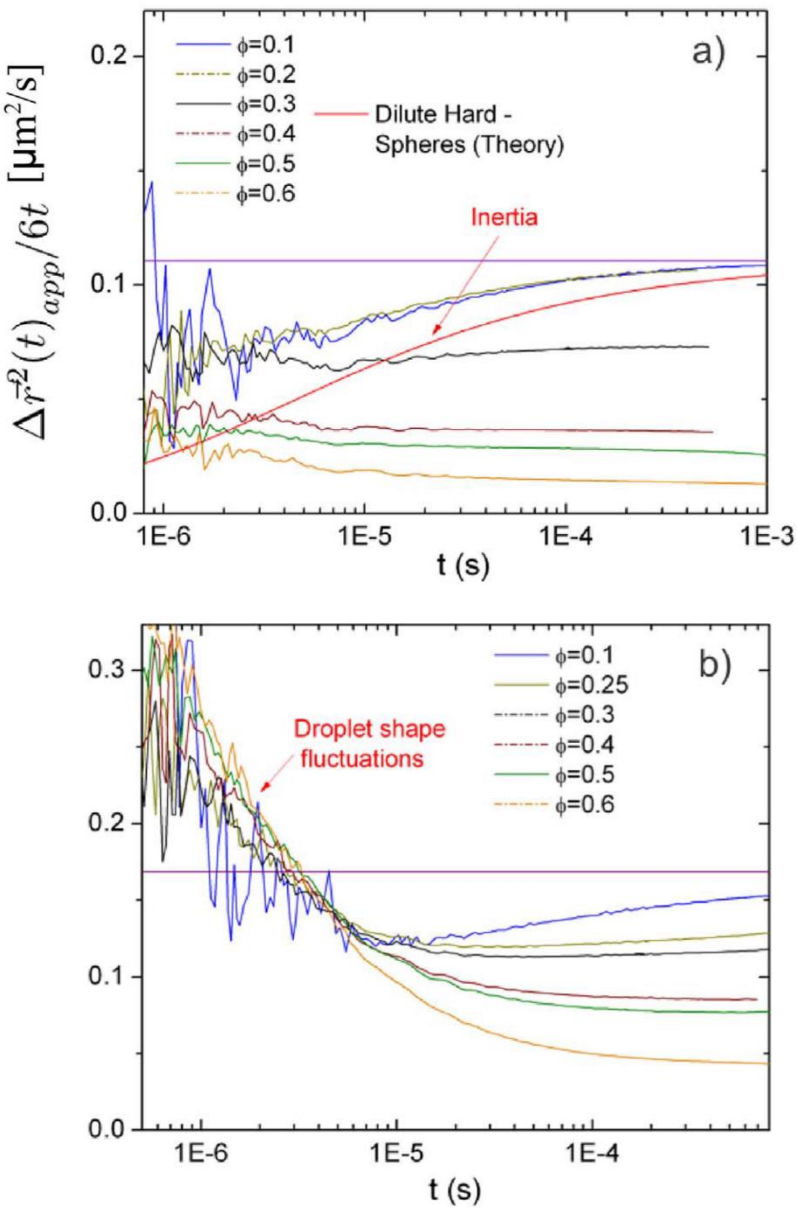

Figure 4.2 Onset of simple diffusive motion as diffusion regime which $\langle \Delta r^2(t) \rangle / 6t$ is constant.

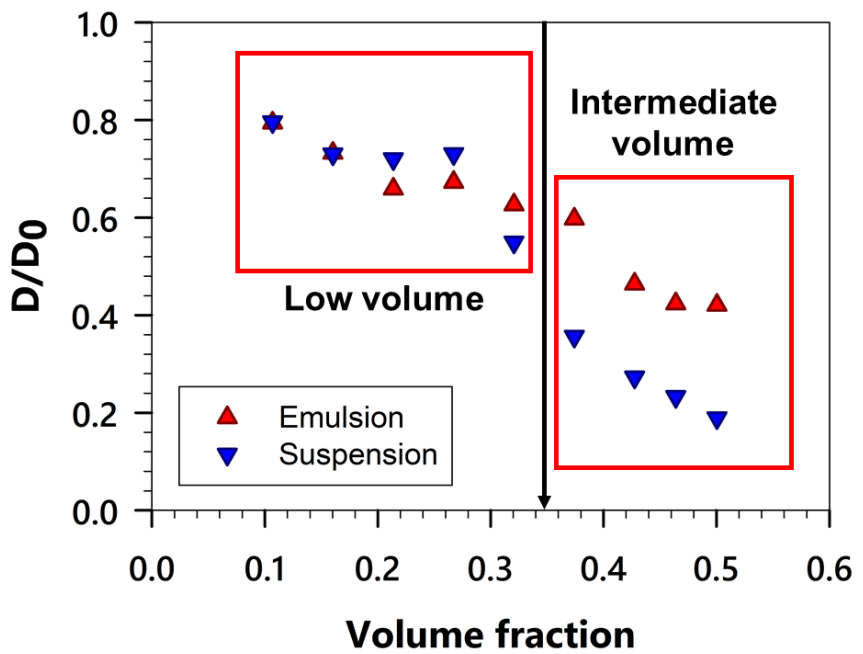

Figure 4.3 Non-dimensionalized diffusion coefficient D/D_0 for set A for both emulsion (red triangle) and suspension (blue inverse triangle). The black line represents the 35 vol%.

4.1.3. Very short time behavior under ϕ_{rcp}

We now turn our attention to the behavior at very short times when approaching typical Brownian time scales, $t_B = m/6\pi\eta R \sim 5 \cdot 10^{-7} s$, characterizing the relaxation of the particle velocity. Here m denotes the mass of the particle and $6\pi\eta R$ is the Stokes friction coefficient. While the MSD data at intermediate time scales are governed by the center of mass diffusion, we observe a dramatic change at short times where strong deviations from the plateau value can be noticed for $t < 10^{-5} s$. Interestingly, for the solid wax particles and the liquid emulsion droplets, the data evolves in opposite directions as mentioned in previous chapters. For the solid wax particles at *T*=15 ℃ the curves tend toward zero for short times while for the liquid droplets at *T*=30 ℃ we detect an upturn at short times. The former is a signature of droplet and fluid inertia [26] while the latter is characteristic for additional thermal fluctuations of the liquid droplet interface. [28,39]

As shown in Figure 4.4, our data for $\phi \geq 0.2$ is well described by Eqs. (2.1) and (2.2), assuming $\langle \Delta \vec{r}^2(t) \rangle / 6t$ as constant. This simplification is justified for the more concentrated emulsions $\phi \geq 0.2$ as can be seen in Figure 4.2 for the case of solid wax particles, i.e. in the absence of shape fluctuations. The relaxation times are found to be of the order 10^{-6} s, and the concentration dependence of τ_{sf} and A shows a noticeable increase with ϕ, observations

that all compare well to the results reported previously for simple emulsions that do not show solidification of the droplets for accessible temperatures, i.e. above the freezing point of the continuous phase $T > 0$ ℃. [28]

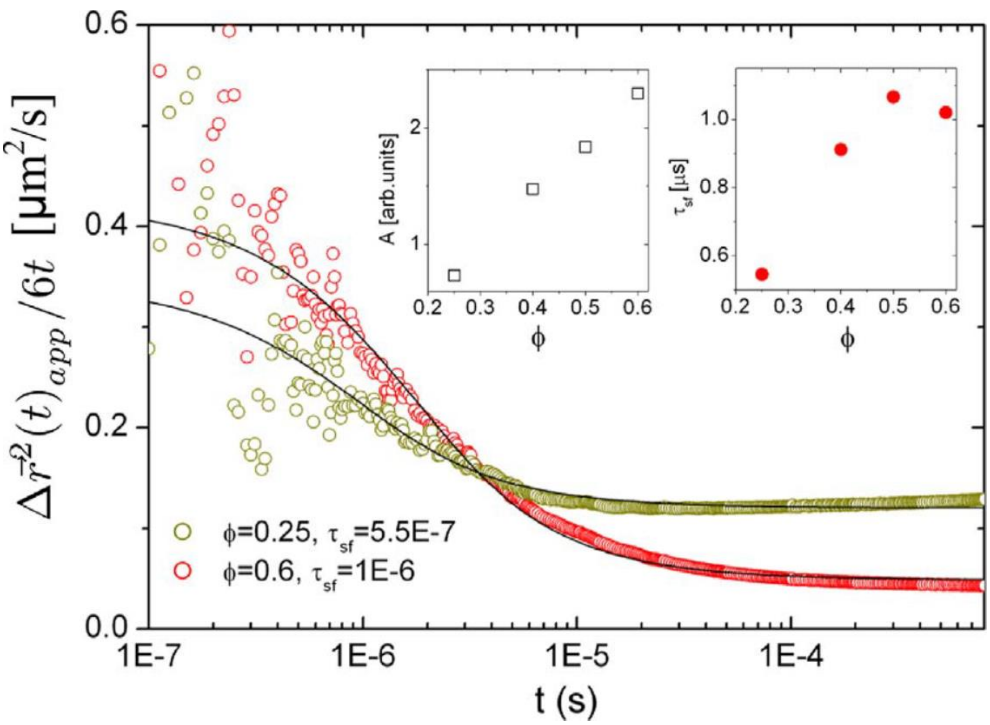

Figure 4.4 Analysis of the contribution of shape fluctuations to the apparent mean square displacement of the droplets at 30 °C. Solid lines are fits to the data with Eq (2.1). Inset: fitting parameters A and τ_{sf} for different droplet volume fractions.

4.1.4. Elasticity index above ϕ_{rcp}

Until now on, we only consider data for $\phi \leq \phi_{rcp}$ where the dispersion is liquid. We note that for concentrations larger than ϕ_{rcp} we do indeed observe the onset of elasticity both in rheology experiments and for DWS. [1,43] Following the definition of EI in Eq (2.3), we plot the Figure 4.5. In Figure 4.5, the volume dependence of the EI is different for suspension and emulsion: for the emulsion the EI continues to increase while the suspension has a limiting value over $\phi \geq 0.65$, and the EI of the suspension is higher than that of emulsion in the whole volume fraction regime.

The increase of EI for the emulsion can be interpreted since the elasticity origin of emulsion comes from the interface of neighboring droplets: as the volume fraction increases, the flat facets between neighboring particles are created more, thus the elasticity index increases by the distortion of particle itself. This is due to the deformable characteristics of the soft particle.

However, for the suspension, even though the particles are also deformed at high volume fraction regime and thus have flat facets at the interfaces, a ready-made facets of the hard particles cannot be deformed anymore once the particles are solidified. This implies that the distorted surface areas for single hard particle are not change despite the osmotic pressure of the system increases: therefore, the EI of the suspension over 65 vol% does not change

as the distortion of a single particle is fixed regardless of the volume fraction as shown in Figure 4.5 blue symbols.

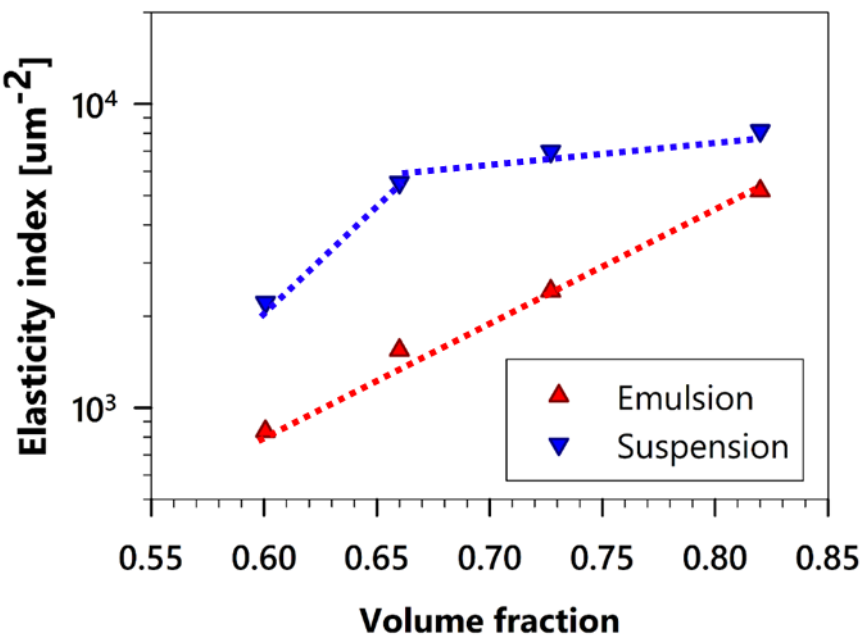

Figure 4.5 Elasiticity index (EI) of the emulsions (red triangle) and suspensions (blue inverse triangle) obtained from DWS.

4.1.5. Scattering transport mean free path l^* under ϕ_{rcp}

Finally, we analyze the results obtained for the optical transport mean free path, Figure 4.6, which is a measure of the light scattering strength or optical density. The latter is a function of the volume fraction ϕ and droplet-droplet positional correlations. [44] Positional correlations and loss of contrast lead to a deviation of the linear scaling of the optical density $1/l^* \propto \phi$.

As we can see from Figure 4.6, such deviations are moderate and both data sets show a steady, nearly linear, increase up to concentrations on the order of ϕ=0.5. This is typically observed for particles with a size significantly larger than the wavelength of light $R \gg \lambda$. [33] Interestingly the slope of $1/l^* \propto \phi$ is slightly higher for the solid wax particles at the lower temperature of T = 15 ℃. This indicates that the individual particle scattering properties change after the α−eicosene has solidified. A possible reason for this change would be a slightly increased particle refractive index when the wax solidifies. [35] The relative refractive index of α−eicosene/water is 1.08 for 30 ℃ and 1.11 for 15 ℃ in detail but still needs some further works to explain the effect of relative refractive index on the slope of reciprocal scattering transport mean free path.

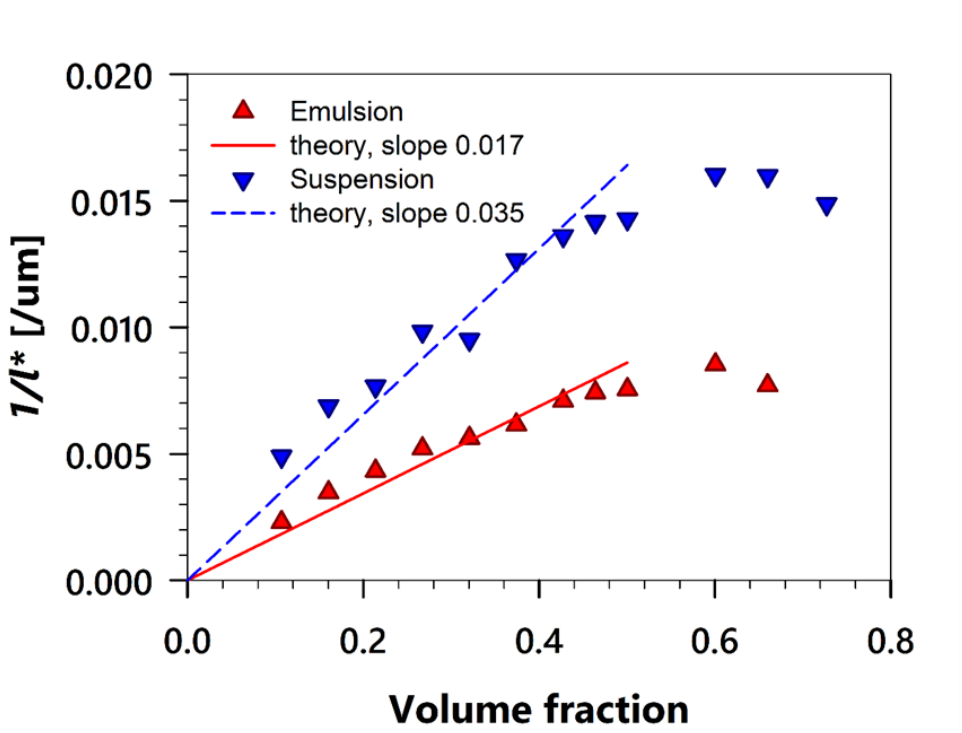

Figure 4.6 Reciprocal optical transport mean free path of the emulsions at T=15 °C and at T=30 °C obtained from diffuse transmission measurements.

4.2. Macroscale analysis

4.2.1. Viscosity for low/intermediate volume fraction regime

In the following we study the properties of suspensions or emulsions for volume fractions ranging from $0.1 \leq \phi \leq \phi_{rcp}$. In Figure 4.7, flow curve of emulsion and suspension is measured for low to intermediate volume fraction regime. While the viscosity of the emulsion diverges at ϕ_{rcp} and the emulsion behaves as solid like materials, under ϕ_{rcp} the non-deformed droplets of emulsion exhibits a simple Newtonian behavior [21,22] and there is no big difference around 35 vol% which coincides well with the data in Figure 4.3 that shows similar trend of decrease. Flow curve of suspension is shown only for the low volume fraction regime in Figure 4.7(b). The viscosity of emulsion and suspension extracted from the Newtonian plateau regime(shear rate 10~100 /s for 30 ℃, 6~60 /s for 15 ℃) in Figure 4.7 is plotted in Figure 4.8 to see the effect of volume fraction on the viscosity.

The viscosity of emulsion under ϕ_{rcp} fits well with the Lionberger and Russel equation Eq (4.1) [45] as shown in Figure 4.8(a). For the η_0 in the Eq (4.1), the water viscosity at 30 ℃ (0.798 cP) is used. The good agreements between the experimental data and the semi-empirical equation means that the wax dispersed system at high temperature behaves as a good

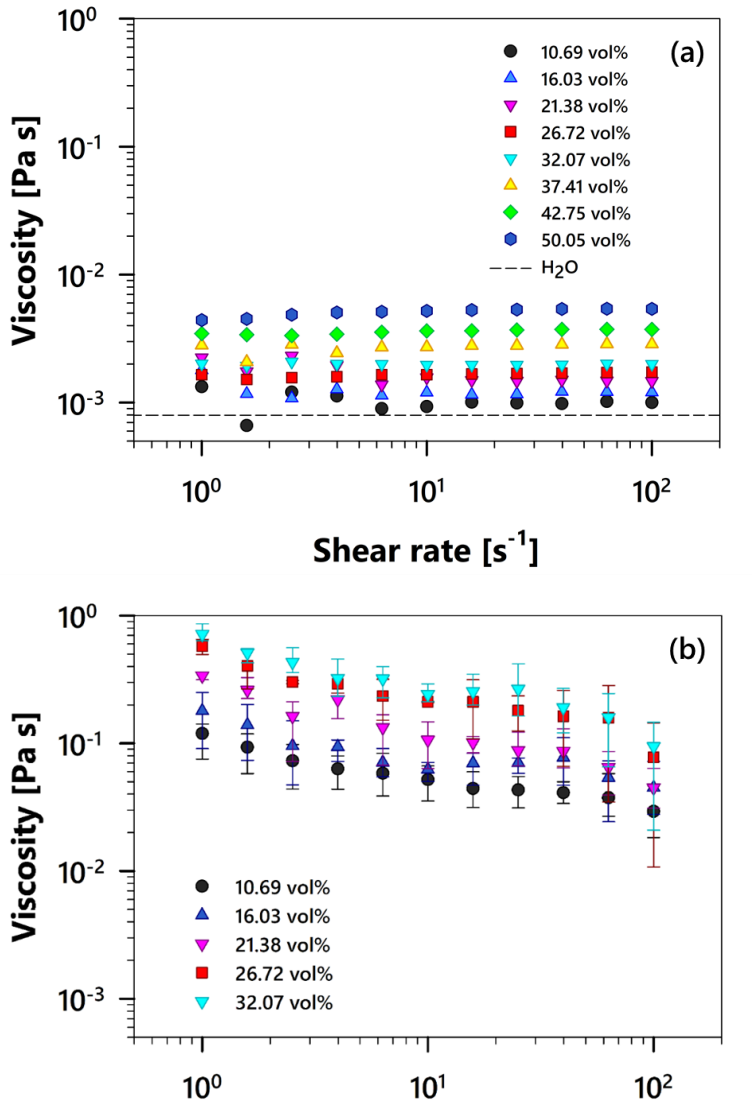

Figure 4.7 (a) Shear flow curves for the emulsion droplets at different volume fractions. The dispersion viscosity is extracted from the data over a shear rate ranging from 10 to 100 /s. (b) Shear flow curves for the suspension particles at different volume fractions. The dispersion viscosity is extracted from the data over a shear rate ranging from 6 to 60 /s.

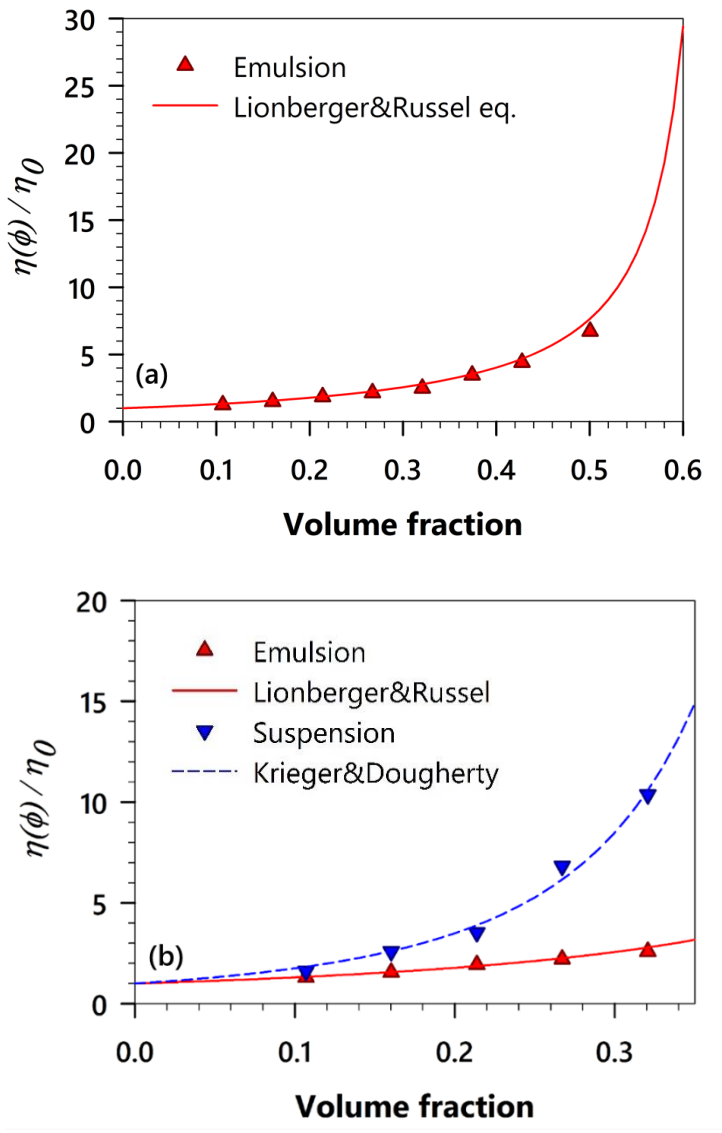

Figure 4.8 (a) Viscosity of the emulsion at 30 °C as a function of the droplet volume fraction (red triangle symbols). Solid line shows the prediction for the semi-empirical expression by Lionberger&Russel. (b) Viscosity of the suspension at 15 °C as a function of the droplet volume fraction (blue inverse triangle symbols). Dashed line shows the prediction for the semi-empirical expression by Krieger&Dougherty.

model emulsion system.

$$\text{Lionberger and Russel}: \ \eta_r = \frac{\eta}{\eta_0} = \frac{1+1.5\phi(1+\phi-0.189\phi^2)}{1-\phi(1+\phi-0.189\phi^2)} \qquad (4.1)$$

For suspension, the viscosity is fitted with the Krieger-Dougherty equation Eq (4.2), which is commonly used in particulate system as in Figure 4.8(b).

$$\text{Krieger and Dougherty}: \ \eta_r = \eta/\eta_0 = (1-\phi/\phi_m)^{-B\phi_m} \qquad (4.2)$$

The fitting parameter for the suspension is $\eta_0 = 27.07$ cP and it shows about 30 times larger gap compared to the water viscosity 1.137 cP at 15 ℃. In other words, the system's viscosity deviates from the expected value as the wax particles is suspended in water. It means that there is an effect of temperature to the interaction between particles and this difference of softness is applied for both low and intermediate volume fraction while the D is affected by interparticle interaction only in the intermediate regime. Meanwhile for the suspension, unlike the emulsion, it behaves like a viscoelastic material in which elastic modulus can be measured for both low and intermediate volume fraction regime. Figure 4.9 shows the result of the strain sweep test of a 50.05 vol% sample as an example. Here the storage modulus and loss modulus have plateau values in low strain regime followed

by a decrease without bumping as strain increases. The size and volume dependence of the system will be analyzed in next chapter with high volume fraction regime data as Figure 4.12 and Figure 4.13.

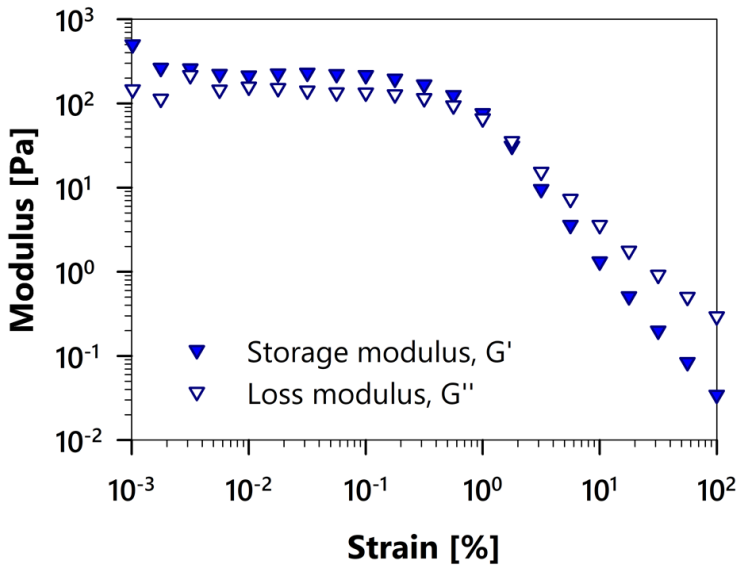

Figure 4.9 Dynamic strain sweep test at frequency = 1 /s for 50.05 vol% sample of set A (*G'* : solid symbols, *G''* : open symbols).

4.2.2. Viscoelastic behavior for high volume fraction regime

Strain sweep and frequency sweep test results of the 86.92 vol% of set B sample (smaller size droplets) are presented as an example for high volume fraction regime in Figure 4.10. In Figure 4.10(a), both emulsion and suspension have linear regime until certain critical strain (defined as the yield strain) but for the suspension it has narrower linear regime and no bumping in loss modulus *G"*, while *G"* of emulsion shows a clear bumping like the model emulsion system. [22] For the suspension of 86.92 vol%, the form of the graph is almost the same with that of the suspension at intermediate volume fraction regime (in Figure 4.9) despite the volume fraction increases and finally exceeds the typical limits, ϕ_{rcp}.

In Figure 4.10(b), the storage and loss modulus are much higher for suspension than those of emulsion. Although the origin of the elasticity in emulsion is changed from thermal fluctuations to the structural disorder of droplets as the volume fraction increases [24], *G'* is always smaller for the emulsion than the suspension. For both emulsion and suspension, *G'* and *G"* is nearly parallel which imply the systems have gel-like network structure. Focusing on the frequency dependence of the emulsion and suspension in Figure 4.10(b), the slope is different: *G'* and *G"* both are almost independent of frequency for the emulsion, while for the suspension, *G'* slightly increases

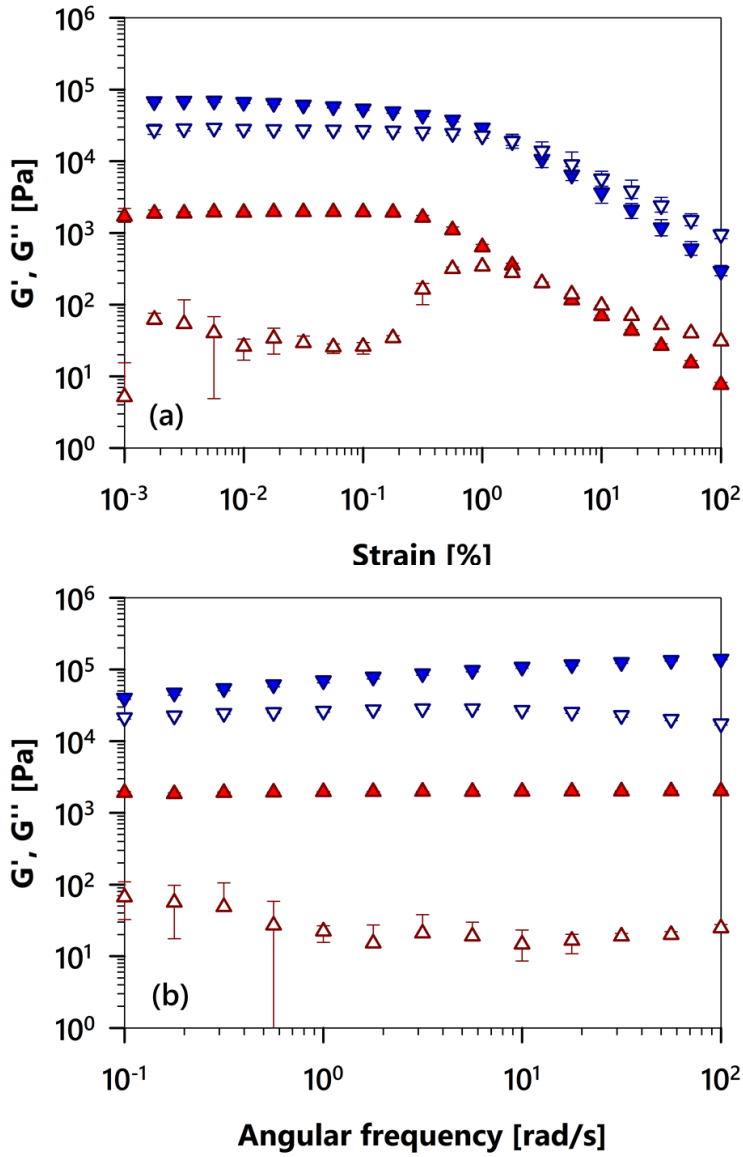

Figure 4.10 (a) Dynamic strain sweep for 86.92 vol% sample of set B at frequency 1 rad/s. (b) Dynamic frequency sweep for 86.92 vol% sample of set B at strain 0.01 % (linear viscoelastic regime). *G'* as solid and *G"* as open symbols while emulsion is represented as red symbol and suspension is represented as blue symbol.

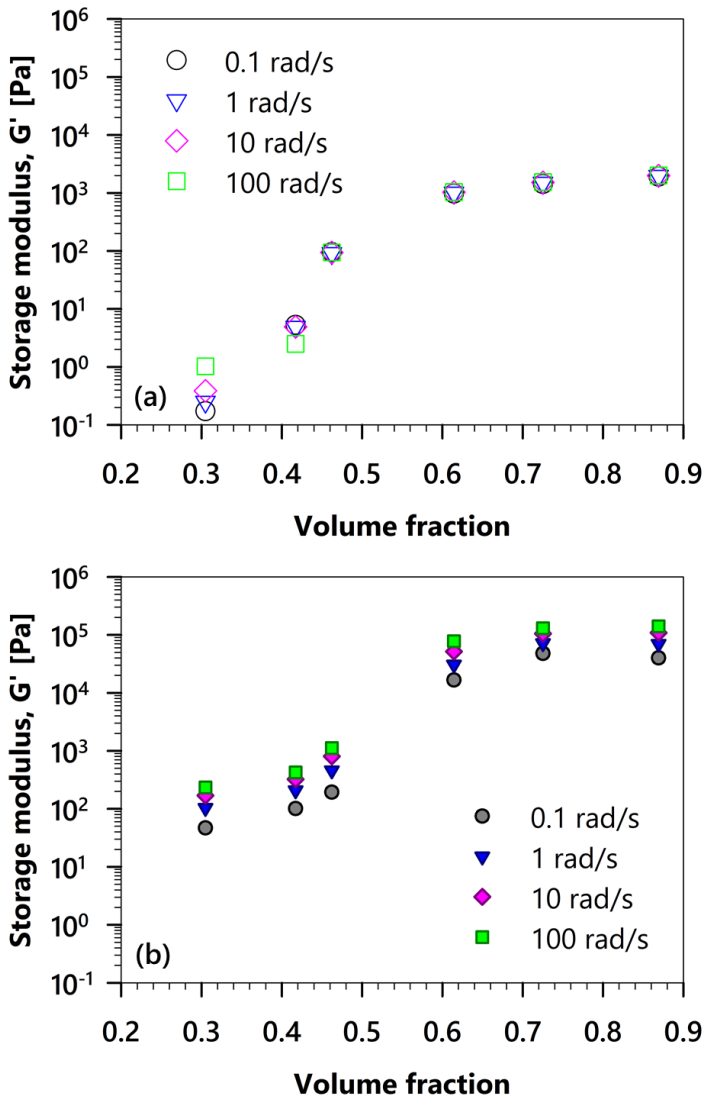

Figure 4.11 Values of storage modulus as a function of volume fraction at frequency = 0.1, 1, 10, 100 rad/s. (a) is for the emulsion and (b) is for the suspension.

with frequency.

To clearly see the difference in the frequency dependence, the storage modulus at frequency=0.1, 1, 10, 100 rad/s are plotted versus volume fraction in Figure 4.11. Both suspension and emulsion show solid-like response in the whole volume fraction regime but follow different frequency dependence. For the emulsion, except low volume fraction regime (under 35 vol%), there is little frequency dependence. Meanwhile for the suspension, both *G'* and *G''* have a clear frequency dependence.

By analogy to the hard sphere system, the elasticity of the emulsion can be represented by a plateau elastic modulus, G_p'. [46] G_p' represented in Figure 4.12 is attained from the strain sweep test at frequency = 1 rad/s in the linear regime for different particle size sample set A and B. For the emulsion, G_p' increases as the volume fraction increases which means the droplets are more and more deformed as the volume fraction increases, and the surface area of the droplets increases which creates additional storage energy by imposing shear deformation at the interface. For the intermediate regime in Figure 4.12, G_p' is higher when the size is smaller and the particles are softer and this shows similar size dependent behavior to that of the emulsion. However, this trend changes for the suspension system: G_p' of the suspension is size independent for the high volume fraction regime.

To quantitatively analyze the size dependency of G_p', we introduce Laplace

pressure $\Pi_L = 2\sigma/a$ to get rid of the size effect in the plateau storage modulus. Usually the scaling is done dividing the G_p' by Laplace pressure Π_L and the expression is like $G_p'/\Pi_L = (G_p' \cdot a)/2\sigma$. Here Set A and B both have the same interfacial tension since the system is based on the same wax (α-eicosene) but the size ratio is about 2 (average diameter of A is twice of that of set B), so that the Laplace pressure ratio between set A and B has the value around 2. Therefore, for simple scaling using Laplace pressure ratio, one could double the data from set B which has smaller size.

By using Laplace pressure ratio, one can get rid of the size effect without knowing the exact value of the surface tension if the system is the same as in this case. Figure 4.13 plots the scaled plateau storage modulus using Laplace pressure ratio for whole volume fraction regime except the high volume fraction regime of the suspension system. The master curve in Figure 4.13 compensating the droplet size effect just by simple scaling using the Laplace pressure ratio can be achieved not only for the emulsion but also for the suspension system. But the size scaling is limited to the low and intermediate volume fraction regime (under ϕ_{rcp}).

For the emulsion, the size dependence is well adjusted using the Laplace pressure ratio for the whole volume fraction regime as shown in Figure 4.13. If we take a close look at the emulsion case, the G_p' shows different tendencies for intermediate and high volume fraction regime. For the

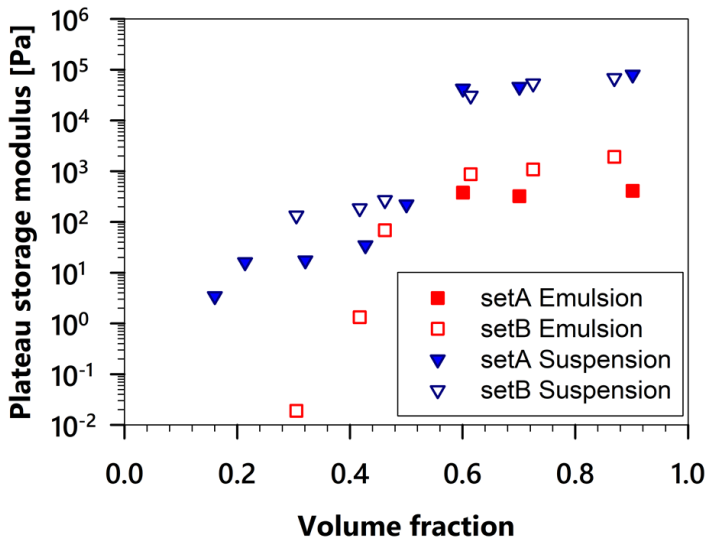

Figure 4.12 Values of plateau storage modulus as a function of volume fraction with emulsion as square symbol and suspension as inverse triangle symbol (unscaled).

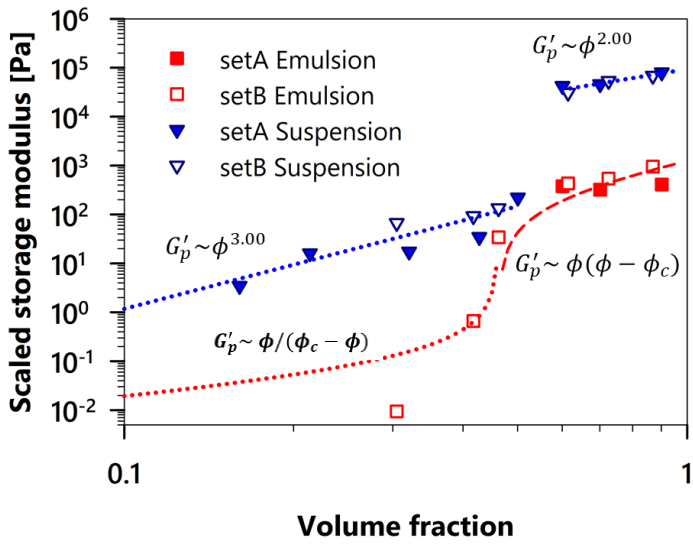

Figure 4.13 Values of scaled plateau storage modulus using Laplace pressure as a function of volume fraction with emulsion as square symbol and suspension as inverse triangle symbol. Blue dotted line under ϕ_{rcp} shows power-law behavior of the suspension, $G_p' \sim \phi^3$ while blue dotted line above ϕ_{rcp} shows power-law behavior of the suspension, $G_p' \sim \phi^2$. Red dotted line follows the model equation $G_p' \sim \phi/(\phi_c - \phi)$ which diverges at ϕ_c, while red dashed line above ϕ_{rcp} follows the network-spring model $G_p' \sim \phi(\phi - \phi_c)$.

intermediate volume fraction regime ($\phi < \phi_{rcp}$), G'_p follows the model equation $G'_p \sim \phi/(\phi_c - \phi)$ which diverges at $\phi_c \sim 0.46$ (Figure 4.13 red dotted line). [47] The parameter ϕ_c, critical volume fraction of 0.46 is used and it shows some deviation from the suggested value of $\phi_c \sim 0.6$ in monodisperse emulsion because of high polydispersity of the sample. For the high volume fraction regime $\phi > \phi_{rcp}$, G'_p follows the network-spring model equation $G'_p \sim \phi(\phi - \phi_c)$ (Figure 4.13 red dashed line) [1] which assumes that the elasticity is entropic in origin. So for the whole volume fraction regime, the α-eicosene emulsion acts as a good model emulsion system. Since the elasticity of the emulsion could be explained as the distortion of particles, the scaling using the Laplace pressure has the same origin as the EI in Figure 4.5. As the particle size increases, the distorted facet area ratio decreases as the Laplace pressure decreases and this is reflected as an increase of EI.

On the other hand, for the suspension case, the size dependence and the concentration dependence of G'_p is changed as the volume fraction increases. For both intermediate and high volume fraction regime, G'_p shows a power law behavior but the factor decreases from 3 to 2 as the concentration increases. For the low and intermediate regime (under ϕ_{rcp}) the size dependence is removed using the Laplace pressure ratio while G'_p is size independent for the high volume fraction regime. However this does not

imply that the suspension and emulsion have the same origin of elasticity: this only indicates that the suspension under ϕ_{rcp} shows size dependence similar to emulsion as inverse to the size.

For the concentrated system above ϕ_{rcp}, the particles should have non-spherical shape for both emulsion and suspension [21] and have facets in their interfaces but the characteristics of the facets are different. For the emulsion, the droplets are soft and the facets could be modified by osmotic pressure caused by increase of volume fraction or shear stress. But the facets in the particle of the suspension is fixed in its shape and cannot be distorted by particle external stresses. The generation of facets in the suspension system could be categorized in two different types: for low and intermediate volume fraction regime, the facet is created by the crystallization process during the solidification expanding radial direction from the center of particles meanwhile for high volume fraction regime, the facet is not only generated by crystallization but also induced by the presence of other neighboring particles. Although both system in high volume regime have facets induced by the presence of other surrounding particles, the two shows different responses to the external pressure and contributes to the elasticity of the system in different way as clearly shown in Figure 4.5.

This difference of facet characteristic also results the difference size dependence of G_p'. For the emulsion, a single droplet is distorted more and

more as the volume fraction increases since the particle surface is deformable, which directly leads to the increase of G_p' in bulk scale and the increase of EI in microscale. As the size of the droplet decreases, the area of the soft facets increases, which can be normalized by the Laplace pressure ratio. Therefore the G_p' proportional to the facet area can be scaled using the Laplace pressure. However, for the suspension at high volume fraction regime, EI representing the elasticity of the particle in microscale does not depend on the volume fraction because the surface is non-deformable, and the facets could not be modified nor regenerated after cooling. This can explain why there is no size dependence for the suspension in high volume fraction regime: no change in facet area after solidification of droplets in emulsion state.

In the analogy to the emulsion, the power law scaling of the suspension at high volume fraction regime could be explained as the approximation of the model equation $G_p' \sim \phi(\phi - \phi_c)$ for the emulsion. If $\phi \gg \phi_c$, then G_p' is approximated to $\phi(\phi - \phi_c) \approx \phi^2$ (in Figure 4.13 blue-dotted line). This kind of approximation cannot explain the different origin of elasticity of emulsion and suspension. Meanwhile the origin of elasticity is different from that of emulsion even though both have the same facets in the interfaces, this difference only be captured in the microscale analysis done by DWS but not in the bulk scale analysis using rheometer.

Chapter 5.

Summary

In conclusion, we have shown that a uniform microscale emulsion of α-eicosene wax droplets dispersed in an aqueous SDS solution is an interesting colloidal model system with tunable properties of constituent droplets from deformable to rigid. Over a wide range of droplet volume fraction, the droplets mimic either the behavior of solid spheres for temperatures below T_c, or the behavior of liquid droplets for temperatures above T_c. By just changing the temperature, the system can alter from emulsion to suspension or vice versa without affecting any other physical properties such as surface tension, size, or volume fraction.

We have shown that DWS can capture the microscopic dynamics at the microsecond scale and we could identify the contribution of center of mass diffusion and shape fluctuations of the liquid droplets over the whole range, consistent with the results from prior studies on non-waxy emulsions. We anticipate that measuring and interpreting early-time DWS data could potentially yield quantitative information about the high frequency viscoelasticity inside the dispersed colloidal objects of different soft materials types, beyond simple hydrocarbon waxes.

Also we could approach to high volume fraction regime for both particulate system, hard and soft, by just changing the temperature of wax suspended system while one cannot approach to the high volume fraction regime above ϕ_{rcp} in ordinary means. This comparison may broaden the scope of the

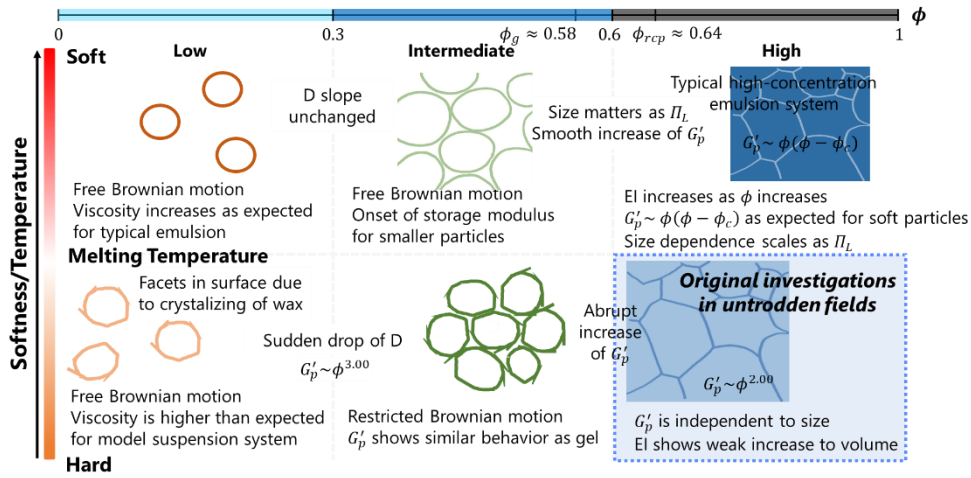

Figure 5.1 Structure representation for both emulsion and suspension over a wide range of volume fraction. The scheme describes how different regime of volume fraction lead to different structural response under shear and microscale diffusive motions.

exploring dynamics for emulsion/suspension for wide range of volume fraction.

Here the system is analyzed using rheometer and DWS, and the result is summarized as the schematic diagram in Figure 5.1. The system's volume fraction regime is categorized into 3 parts to understand the system in detail: low volume fraction regime (up to 35 vol%), intermediate volume fraction regime (35 vol% ~ϕ_{rcp}), and finally the high volume fraction regime (above ϕ_{rcp}). Criteria for the classification is determined using systems' micro/macroscopic characteristics.

Around 35 vol%, which indicates change from the low to the intermediate volume fraction regime, the slope of diffusion coefficient suddenly drops only for suspension and stays the same for emulsion. This implies that the change of the particle surface softness plays a significant role in suspension system for intermediate volume fraction regime even though they still do not contact each other. However, this microscopic change is not reflected in the bulk scale properties attained from the rheological data. For both low and intermediate volume fraction regime, emulsion acts as a good model system following Lionberger&Russel equation and suspension has plateau storage modulus due to the facets induced by the crystallization process when solidifying.

The solidification of the α-eicosene wax and the subsequent shape changes may complicate the use of this material for testing models and concepts of the

glass and the jamming transition in even denser suspensions, for $\phi > \phi_{rcp} \sim 0.64$. Thus, the reversibility of the transition is limited only over certain time scales after the temperature change, since the droplets can evolve into faceted or disc-like shapes. Moreover, in tandem with the faceting of the particles, solidification driven shape-changes of particles may alter particle–particle interactions, potentially leading to a weakly attractive component that may depend on the shapes and orientations of interacting wax particles.

Around ϕ_{rcp}, which is empirical parameter of hard monodisperse particle system characterizing the maximum volume fraction obtained when they are packed randomly, both emulsion and suspension act as a gel-like system but the details in rheological properties and the microscopic movement are somewhat different. For emulsion, as volume fraction increases, the droplets deform more and more and the facet area of single particle also increases. This is reflected in the increase of EI for single particle, and as the origin of elasticity comes from the structural disorder of droplets, the G_p' is size-dependent because as the size bigger, more deformation can occur. However, for the suspension, the facet area could not be newly created after the generation of facets during the solidifying process even if the volume fraction increases. Therefore the G_p' is size independent in this case because the characteristic of facets is different from that of emulsion.

To our best understanding, this is the first time presenting the physical

properties of suspension for high volume fraction. From this work, we could observe the high volume fraction suspension system above ϕ_{rcp} and its response to the external shear. Unlike the emulsion, it shows dramatic changes at the ϕ_{rcp} and the plateau storage modulus is independent to the size of droplet and is only affected by the volume fraction.

Bibliography

[1] T.G. Mason, J. Bibette, D.A. Weitz, Elasticity of compressed emulsions, Phys. Rev. Lett. 75 (1995) 2051–2054. doi:10.1103/PhysRevLett.75.2051.

[2] E. N, Encyclopedia of Emulsion Technology , Pharm. Unserer Zeit. (1984). doi:10.1002/pauz.19840130212.

[3] G.M. Conley, P. Aebischer, S. Nöjd, P. Schurtenberger, F. Scheffold, Jamming and overpacking fuzzy microgels: Deformation, interpenetration, and compression, Sci. Adv. (2017). doi:10.1126/sciadv.1700969.

[4] P.S. Mohanty, S. Nöjd, K. Van Gruijthuijsen, J.J. Crassous, M. Obiols-Rabasa, R. Schweins, A. Stradner, P. Schurtenberger, Interpenetration of polymeric microgels at ultrahigh densities, Sci. Rep. (2017). doi:10.1038/s41598-017-01471-3.

[5] A. Fernandez-Nieves, H.M. Wyss, J. Mattsson, D.A. Weitz, Microgel Suspensions: Fundamentals and Applications, 2011. doi:10.1002/9783527632992.

[6] M. Braibanti, H.S. Kim, N. Şenbil, M.J. Pagenkopp, T.G. Mason, F. Scheffold, The liquid-glass-jamming transition in disordered ionic nanoemulsions, Sci. Rep. (2017). doi:10.1038/s41598-017-13584-w.

[7] P.N. Pusey, W. Van Megen, Phase behaviour of concentrated suspensions of nearly hard colloidal spheres, Nature. (1986). doi:10.1038/320340a0.

[8] G. Brambilla, D. El Masri, M. Pierno, L. Berthier, L. Cipelletti, G. Petekidis, A.B. Schofield, Probing the equilibrium dynamics of

colloidal hard spheres above the mode-coupling glass transition, Phys. Rev. Lett. (2009). doi:10.1103/PhysRevLett.102.085703.

[9] K.N. Pham, G. Petekidis, D. Vlassopoulos, S.U. Egelhaaf, P.N. Pusey, W.C.K. Poon, Yielding of colloidal glasses, Europhys. Lett. (2006). doi:10.1209/epl/i2006-10156-y.

[10] A.P. Gast, W.B. Russel, Simple Ordering in Complex Fluids, Phys. Today. (1998). doi:10.1063/1.882495.

[11] P. Bartlett, R.H. Ottewill, P.N. Pusey, Freezing of binary mixtures of colloidal hard spheres, J. Chem. Phys. (1990). doi:10.1063/1.459142.

[12] W.C.K. Poon, E.R. Weeks, C.P. Royall, On measuring colloidal volume fractions, Soft Matter. (2012). doi:10.1039/c1sm06083j.

[13] J.R. Seth, L. Mohan, C. Locatelli-Champagne, M. Cloitre, R.T. Bonnecaze, A micromechanical model to predict the flow of soft particle glasses, Nat. Mater. 10 (2011) 838–843. doi:10.1038/nmat3119.

[14] A. Ikeda, L. Berthier, P. Sollich, Disentangling glass and jamming physics in the rheology of soft materials, Soft Matter. (2013). doi:10.1039/c3sm50503k.

[15] A.J. Liu, S.R. Nagel, The Jamming Transition and the Marginally Jammed Solid, Annu. Rev. Condens. Matter Phys. (2010). doi:10.1146/annurev-conmatphys-070909-104045.

[16] P. Olsson, S. Teitel, Critical scaling of shear viscosity at the jamming transition, Phys. Rev. Lett. (2007). doi:10.1103/PhysRevLett.99.178001.

[17] H.A. Barnes, Rheology of emulsions — a review, Colloids Surfaces A Physicochem. Eng. Asp. 91 (1994) 89–95. doi:10.1016/0927-7757(93)02719-U.

[18] N. Koumakis, a. Pamvouxoglou, a. S. Poulos, G. Petekidis, Direct comparison of the rheology of model hard and soft particle glasses, Soft Matter. 8 (2012) 4271. doi:10.1039/c2sm07113d.

[19] C. Pellet, M. Cloitre, The glass and jamming transitions of soft polyelectrolyte microgel suspensions, Soft Matter. (2016). doi:10.1039/c5sm03001c.

[20] M.N. Lee, H.K. Chan, A. Mohraz, Characteristics of pickering emulsion gels formed by droplet bridging, Langmuir. 28 (2012) 3085–3091. doi:10.1021/la203384f.

[21] T.G. Mason, J.N. Wilking, K. Meleson, C.B. Chang, S.M. Graves, Nanoemulsions: formation, structure, and physical properties, J. Phys. Condens. Matter. 18 (2006) R635–R666. doi:10.1088/0953-8984/18/41/R01.

[22] T.G. Mason, J. Bibette, D.A. Weitz, Yielding and flow of monodisperse emulsions, J. Colloid Interface Sci. 179 (1996) 439–448. doi:10.1006/jcis.1996.0235.

[23] J. Mewis, N.J. Wagner, Colloidal suspension rheology, 2011. doi:10.1017/CBO9780511977978.

[24] T. Mason, M.-D. Lacasse, G. Grest, D. Levine, J. Bibette, D. Weitz, Osmotic pressure and viscoelastic shear moduli of concentrated emulsions, Phys. Rev. E. 56 (1997) 3150–3166. doi:10.1103/PhysRevE.56.3150.

[25] D.A. Weitz, D.J. Pine, P.N. Pusey, R.J.A. Tough, Nondiffusive Brownian motion studied by diffusing-wave spectroscopy, Phys. Rev. Lett. (1989). doi:10.1103/PhysRevLett.63.1747.

[26] E.J. Hinch, Application of the Langevin equation to fluid suspensions, J. Fluid Mech. (1975).

doi:10.1017/S0022112075003102.

[27] R. Huang, I. Chavez, K.M. Taute, B. Lukić, S. Jeney, M.G. Raizen, E.L. Florin, Direct observation of the full transition from ballistic to diffusive Brownian motion in a liquid, Nat. Phys. (2011). doi:10.1038/nphys1953.

[28] H. Gang, A.H. Krall, D.A. Weitz, Shape fluctuations of interacting fluid droplets, Phys. Rev. Lett. 73 (1994) 3435–3438. doi:10.1103/PhysRevLett.73.3435.

[29] L.F. Rojas-Ochoa, D. Lacoste, R. Lenke, P. Schurtenberger, F. Scheffold, Depolarization of multiple scattered reflected light, AIP Conf. Proc. (2007). doi:10.1063/1.2563188.

[30] J. Bergenholtz, W.C.K. Poon, M. Fuchs, Gelation in Model Colloid - Polymer Mixtures, Langmuir. 19 (2003) 4493–4503.

[31] C. Tisserand, M. Fleury, L. Brunel, P. Bru, G. Meunier, Passive microrheology: Non intrusive measurement of emulsion and suspension stability, in: Nanotechnol. 2011 Adv. Mater. CNTs, Part. Film. Compos. - 2011 NSTI Nanotechnol. Conf. Expo, NSTI-Nanotech 2011, 2011.

[32] J.P. Hansen, I.R. McDonald, Theory of Simple Liquids, 2006. doi:10.1016/B978-0-12-370535-8.X5000-9.

[33] S. Fraden, G. Maret, Multiple light scattering from concentrated, interacting suspensions, Phys. Rev. Lett. (1990). doi:10.1103/PhysRevLett.65.512.

[34] W.M. Haynes, CRC Handbook of Chemistry and Physics 95th Edition (Internet Version 2015), CRC/Taylor Fr. (2015). doi:10.1136/oem.53.7.504.

[35] T.G. Mason, Osmotically driven shape-dependent colloidal

separations, Phys. Rev. E - Stat. Physics, Plasmas, Fluids, Relat. Interdiscip. Top. 66 (2002) 4. doi:10.1103/PhysRevE.66.060402.

[36] F. Scheffold, J.N. Wilking, J. Haberko, F. Cardinaux, T.G. Mason, The jamming elasticity of emulsions stabilized by ionic surfactants, Soft Matter. 10 (2014) 5040–5044. doi:10.1039/c4sm00389f.

[37] A.F. Mejia, P. He, D. Luo, M. Marquez, Z. Cheng, Uniform discotic wax particles via electrospray emulsification, J. Colloid Interface Sci. (2009). doi:10.1016/j.jcis.2009.02.044.

[38] J. Bibette, Depletion interactions and fractionated crystallization for polydisperse emulsion purification, J. Colloid Interface Sci. 147 (1991) 474–478. doi:10.1016/0021-9797(91)90181-7.

[39] H. Gang, A.H. Krall, D.A. Weitz, Thermal fluctuations of the shapes of droplets in dense and compressed emulsions, Phys. Rev. E. 52 (1995) 6289–6302. doi:10.1103/PhysRevE.52.6289.

[40] F. Scheffold, P. Schurtenberger, Light Scattering Probes of Viscoelastic Fluids and Solids, Soft Mater. 1 (2003) 139–165. doi:10.1081/SMTS-120022461.

[41] Brown W, Dynamic Light Scattering: The Method and Some Applications, 16 Diffus. Spectrosc. (1993). doi:10.1093/gerona/glv052.

[42] C. Zhang, M. Reufer, D. Gaudino, F. Scheffold, Improved diffusing wave spectroscopy based on the automatized determination of the optical transport and absorption mean free path, Korea Aust. Rheol. J. (2017). doi:10.1007/s13367-017-0025-z.

[43] D.J. Pine, D.A. Weitz, P.M. Chaikin, E. Herbolzheimer, Diffusing wave spectroscopy, Phys. Rev. Lett. (1988). doi:10.1103/PhysRevLett.60.1134.

[44] L.F. Rojas-Ochoa, S. Romer, F. Scheffold, P. Schurtenberger, Diffusing wave spectroscopy and small-angle neutron scattering from concentrated colloidal suspensions, Phys. Rev. E - Stat. Physics, Plasmas, Fluids, Relat. Interdiscip. Top. (2002). doi:10.1103/PhysRevE.65.051403.

[45] A.J. Banchio, G. Nägele, Short-time transport properties in dense suspensions: From neutral to charge-stabilized colloidal spheres, J. Chem. Phys. 128 (2008) 104903. doi:10.1063/1.2868773.

[46] T.G. Mason, New fundamental concepts in emulsion rheology, Curr. Opin. Colloid Interface Sci. 4 (1999) 231–238. doi:10.1016/S1359-0294(99)00035-7.

[47] S.S. Datta, D.D. Gerrard, T.S. Rhodes, T.G. Mason, D.A. Weitz, Rheology of attractive emulsions, Phys. Rev. E. 84 (2011) 041404. doi:10.1103/PhysRevE.84.041404.

국문 초록

본 논문에서는 소듐 도데실 설페이트(SDS)를 이용해 유화시킨 1-에이코젠 왁스 현탁액을 콜로이드 모델 시스템으로 이용하여 브라운 열 운동 및 시스템의 유변학적 거동을 분석하였다. 1-에이코젠이 24.6 ℃의 녹는점을 가지므로 1-에이코젠 왁스 현탁액은 녹는점 이하의 온도로 냉각시킬 경우 마이크론 사이즈의 입자가 고화되어 분산 미립자 시스템으로 간주할 수 있다. 한편 녹는점 이상에서는 왁스가 녹아 부드러운 입자로 존재하므로 좋은 모델 유액이 된다. 따라서 단순히 온도만 조절하면서 분산된 입자의 표면 성질이 변화하고, 이에 따라 입자 시스템의 성질도 달라지게 된다.

본 연구에서는 T = 10/15 ℃와 T = 30 ℃의 두 가지 온도에서 다양한 농도의 1-에이코젠 현탁액의 동적 특성과 광학 특성을 분석하였다. 실험 온도는 왁스의 녹는점과 충분히 먼 온도를 택하여 시스템의 안정성을 확보하였다. 이러한 시스템 하에서 두 종류의 장비를 사용하여 입자의 표면의 경도가 온도에 따라 변화함에 따라 시스템의 미세구조 및 거시 구조에 미치는 영향을 다양한 스케일에서 분석할 수 있었다.

먼저 분산된 콜로이드 입자의 소규모 운동 및 형태 변동을 파악하기 위해 확산 광파 분광법 (DWS)의 다중 광 산란 기술을 사용하였다. 녹는점보다 높은 온도에서는 액적의 계면이 분자의

열운동 에너지에 의해 표면 파동을 가지게 되고, 이에 따른 움직임은 매우 짧은 시간 스케일에서의 강도-강도 상관함수에 반영된다. 한편 녹는점보다 낮은 온도의 경우에는 질량 중심 이동외에 표면 파동은 존재하지 않으므로 앞의 경우와 다른 강도-강도 상관함수를 가지게 된다. 또한 이러한 강도-강도 상관함수는 입자의 평균제곱거리에서의 정체기 데이터를 이용하면 점탄성 시스템의 기계적 성질을 결정하는 데도 사용될 수 있다. 이 시스템에서의 액적의 상 변화는 가역적이므로 미세 입자의 표면 성질이 더욱 중요한 영향을 주는 고농도 현탁액에서의 상 변화에 흥미로운 관점을 제시할 수 있다.

이러한 고농도를 포함하여 시스템의 체적분율 범위는 크게 세 가지 범위로 분류될 수 있다. 첫째로 저체적분율 영역을 35 vol% 이하로 정의할 수 있다. 이 영역에서는 확산 계수가 농도에 따라 감소하는 양상을 보이나 입자의 표면 유연성이 영향을 미치지 않는다. 입자의 유연성은 거시적 특성인 점도의 변화에서 관찰된다. 둘째로 중간 체적분율은 35 vol%에서 임의적 조밀쌓임 체적분율까지로 정의할 수 있다. 이때 확산계수는 유액과 현탁액에서 큰 차이를 보이기 시작하며, 거시적 관점에서는 현탁액의 경우 저장 탄성률 등을 통해 고체에 가까워진다. 마지막으로 임의적 조밀 쌓임 체적분율 이상의 농도 범위는 고체적분율 영역으로 정의된다. 임의적 조밀 쌓임 체적분율 이상의 농도를 가질 수 없는 기존의 현탁액들과 달리, 1-에이코젠 현탁액은 고농도 유액의 온도를 낮혀서 고체적분율에 쉽게

도달할 수 있다. 이때 시스템은 체적분율의 손실 혹은 액적 크기의 변화 없이 현탁액으로 변한다.

광범위한 체적분율에서 유변학적 거동을 조사함으로써 입자의 표면 성질이 미세/거시 구조에서의 동역학에 미치는 영향을 파악할 수 있었다. 이 연구를 통해 이전에는 연구된 적 없는 높은 체적분율에서의 현탁액 및 유액의 거동을 이해할 수 있고, 유액과 현탁액의 비교를 통해 표면의 유연성이 미치는 영향을 파악할 수 있었다.

주요어 : 왁스, 현탁액, 유액, 유액의 유변학적 거동, 표면성질 변화

학 번 : 2012 – 20963